Journal of Non-Crystalline Solids 615 (2023) 122426

Contents lists available at ScienceDirect

Journal of Non-Crystalline Solids

journal homepage: www.elsevier.com/locate/jnoncrysol

Comparison of five empirical potential models for aluminosilicate systems: Albite and anorthite as test cases

Annalisa Pallini [a], Marco Bertani [a], Daniel Rustichelli [a], Benedikt Ziebarth [b], Wolfgang Mannstadt [b], Alfonso Pedone [a,*]

[a] Department of Chemical and Geological Sciences, University of Modena and Reggio Emilia, Modena, Italy
[b] SCHOTT AG, Mainz, Germany

ARTICLE INFO

Keywords:
Interatomic potentials
MD simulations
Albite
Anorthite
Aluminosilicate glasses
Thermomechanical properties

ABSTRACT

In this work we have carried out a systematic investigation of the performance of different force fields in correctly reproducing the structure, densities as a function of temperature and the properties (Young's and Bulk moduli and the coefficient of thermal expansion) of both albite and anorthite crystals and glasses. After this first step of comparison, we selected the potential which gave the better overall performances (the Bertani-Menziani-Pedone potential) and investigated the effect of the cooling rate on structure and properties of albite and anorthite glasses and verified the predicting power of MD simulations for the simulation of the coefficient of thermal expansion (CTE) for a series of several aluminosilicate glasses whose compositions go from the albite-like one to the anorthite-like one.

The tested interatomic potentials provide reliable short-range order around the constituting cations, but some differences are detected in the medium-range order described by the T-O-T angles (T= network formers cations, Si and Al), the Al/Si distributions and Q^n distributions. In general, all the potentials overestimate the CTE because of the high quenching rate used but we have shown that extrapolated properties at room temperature provide a more reliable comparison with experiments. The CTE trend of the albite-anorthite plagioclase glass series is well reproduced and associated with the substitution of Na with Ca ions rather than the Al/Si one. The error associated with the computed CTE values decreases with box dimension and we found that simulation boxes containing 50k atoms are necessary to reliably estimate this property.

1. Introduction

Aluminosilicate glasses are steady candidates for the design and development of industrial formulations with interesting and considerable properties.

Indeed, the high scratch resistance and high cracking load make aluminosilicate glasses ideal for producing protective cases for electronic devices such as smartphones and tablets; their resistance to high temperatures, low expansion coefficient, and resistance to chemical and thermal degradation give them also valuable properties for electronic or electrochemical devices [1,2], halogen lamps, high-temperature thermometers, combustion pipes and for the confinement of nuclear wastes.

The development of new technical glasses suitable for several high-tech applications requires quantitative knowledge of the relationships between composition, structure, and properties.

Classical Molecular Dynamics (CMD) simulations allow to perform *in-silico* experiments, analyze how the atomic structure is influenced by the composition, and how it determines properties such as ionic conductivity, mechanical properties, thermal expansion coefficient, etc.… [3,4] Therefore, MD represents a powerful tool to predict, screen and validate innovative glass compostions.

However, it is well known that the key ingredient affecting the accuracy of MD simulations is the interatomic potential model employed, the so-called Force-Fields [5]. In the last decades, several interatomic potential models have been developed for silicate and aluminosilicate glasses [5–10] but a systematic investigation of their accuracy and how they compare to each other is still missing.

This work focuses on the comparison of different potentials on two prototype aluminosilicate crystals, albite, and anorthite, and their corresponding glasses.

Albite [11] (AL) is a feldspar with the formula $NaAlSi_3O_8$ ($2NaAlSi_3O_8 = Na_2O{\cdot}Al_2O_3{\cdot}6SiO_2$) and its crystalline system is pinacoidal

* Corresponding author.
E-mail address: alfonso.pedone@unimore.it (A. Pedone).

https://doi.org/10.1016/j.jnoncrysol.2023.122426
Received 13 March 2023; Received in revised form 15 May 2023; Accepted 26 May 2023
Available online 30 May 2023

Table 1
Glass compositions: percentage of oxides, number of atoms, density.

	Na_2O %	Al_2O_3%	SiO_2 %	Na atoms	Al atoms	Si atoms	O atoms	Exp. Density
Albite	12.5	12.5	75	769	769	2308	6154	2.38
	CaO %	Al_2O_3%	SiO_2 %	Ca atoms	Al atoms	Si atoms	O atoms	Exp. Density
Anorthite	25	25	50	770	1540	1540	6160	2.70

tricline (P-1). Albite crystals are often twinned, and their dress is always crystalline, euhedral or subeudral, with tabular and prismatic crystals. Albite has a vitreous luster and it can be colorless, yellow, white, green, brownish, or black. It is one of the major constituents of granitic rocks and it is in a great fraction of magmatic ones. Together with anorthite, it forms the series of plagioclase; both allow the formation of solid solutions with orthoclase ($KAlSi_3O_8$), which is distinguishable to the naked eye from them.

Anorthite [12] (AN) is a feldspar with the formula $CaAl_2Si_2O_8$ ($CaAl_2Si_2O_8 = CaO{\cdot}Al_2O_3{\cdot}2SiO_2$) and its crystalline system is pinacoidal tricline (P-1). It can be colorless, white, or pinkish and it has a vitreous luster. As mentioned before, anorthite is present in isomorphic mixtures of plagioclase, and, orthoclase whose fraction depends on the amount of aluminum, which replaces silicon in tetrahedral units creating a charge imbalance.

Plagioclase feldspars, particularly albite, and anorthite, are abundant in Earth's crust and their presence influences a lot of its features: e.g., elastic and frictional properties are important for the Earth's crust's seismic prediction and the interpretation of earthquakes' magnitude [2,13,14].

The great importance of these two minerals in nature is transmitted in the same importance that aluminosilicate glasses have in the industrial scenario. They withstand high temperatures (these glasses can be directly used on the flame), and they are used as advanced materials for aircraft, constructions, electronic packaging, and touch screens, for the storage of nuclear wastes, and the production of various glass ceramics. For this reason, in the last part of the article, we will investigate the properties of a series of glasses whose compositions start with the albite-like one and end with the anorthite-like one, passing through four different mixing compositions [15].

From a compositional point of view, alkali aluminosilicate glasses show a decrease in non-bridging oxygens' concentration when Al_2O_3 is added, being that the oxygens introduced with the M_2O may now be employed in the formation of AlO_4 tetrahedra. When the ratio $[M_2O]/[Al_2O_3]$ is less than 1, aluminum starts behaving as network modifiers (with a coordination number of 5 and 6). This kind of glass, together with alkaline earth, is one of the most required and their production covers a large slice of the market.

One of the computational consequences of the scientific and technological interest in aluminosilicate glasses [16], and other oxide glasses, was a rich proliferation of empirical potentials. These potentials differ from one to the other for how they represent atoms (e.g., rigid ion model, core-shell model, polarizable ion model, and so on) and for the complexity of their functional forms that may involve two or many-bodies interactions. The potentials also differ for the kind of parameters that can be fixed or variable with the composition of the glass and for the way of obtaining them [6].

We decided to test five interatomic potential models developed in the last years which comprise parameters for a large variety of cations and are among the most used because of their effectiveness: BMP [8], PMMCS [7], SHIK [9], Du [6], and core-shell [10] (the first four potentials bear in their signature the first letters of their developers' surname).

In the next section, we describe the force fields examined, the computational protocol, and the theoretical background used in the computation of glass properties. Subsequently, all the results are listed and discussed and, to conclude, the last section summarizes the observations and pros and cons for each force field.

2. Computational method

2.1. Force-Fields (FFs) description

2.1.1. BMP potential [8]

The BMP potential has been developed in recent years in the research group of Professor Pedone as an extension of the foregoing PMMCS potential. BMP describes the interactions between ions in a great number of multicomponent oxide-based systems, from crystalline to glassy ones (for the elements and the associated parameters used in this work see Table 1 of the ESI). It is based on the rigid ion model and makes use of three different functional forms to describe the interactions: a (Coulomb-)Morse potential, a Buckingham potential, and a three-bodies

Table 2
First coordination sphere for former cations in albite and anorthite glasses. The radial cutoffs used for Si and Al to determine the coordination numbers are 2.0 and 2.1 Å, respectively.

	Albite PMMCS	BMP	SHIK	Du	CS
Si-coordination					
% Si four-coord.	99.88 ± 0.03	99.74 ± 0.04	99.93 ± 0.04	99.99 ± 0.02	99.65 ± 0.09
Al-coordination					
% Al three-coord.	4.56 ± 0.41	5.94 ± 0.11	1.85 ± 0.23	8.15 ± 0.71	3.85 ± 0.46
% Al four-coord.	94.54 ± 0.53	93.98 ± 0.13	97.62 ± 0.23	91.72 ± 0.67	96.09 ± 0.40
% Al five-coord.	0.84 ± 0.18	0.04 ± 0.05	0.53 ± 0.07	0.06 ± 0.05	0.04 ± 0.06
	Anorthite PMMCS	BMP	SHIK	Du	CS
Si-coordination					
% Si four-coord.	99.84 ± 0.01	99.66 ± 0.07	99.61 ± 0.13	99.99 ± 0.02	99.67 ± 0.03
Al-coordination					
% Al three-coord.	5.95 ± 0.29	5.59 ± 0.46	0.89 ± 0.07	4.05 ± 0.42	2.69 ± 0.42
% Al four-coord.	90.36 ± 0.65	93.88 ± 0.41	95.12 ± 0.63	95.65 ± 0.41	97.30 ± 0.41
% Al five-coord.	3.55 ± 0.42	0.45 ± 0.09	3.97 ± 0.58	0.25 ± 0.02	0.00 ± 0.00

Table 3
Oxygen speciation in albite and anorthite glass.

	Albite PMMCS	BMP	SHIK	Du	CS
% BO	92.42 ± 0.29	94.85 ± 0.08	93.29 ± 0.32	93.46 ± 0.15	96.37 ± 0.20
% NBO	4.01 ± 0.11	2.99 ± 0.04	3.43 ± 0.16	3.78 ± 0.06	2.08 ± 0.10
% TBO	3.55 ± 0.16	2.15 ± 0.03	3.28 ± 0.17	2.76 ± 0.11	1.57 ± 0.09
	Anorthite PMMCS	BMP	SHIK	Du	CS
% BO	79.78 ± 0.76	87.00 ± 0.54	74.55 ± 0.11	85.42 ± 0.29	88.39 ± 0.59
% NBO	10.41 ± 0.36	7.20 ± 0.34	11.87 ± 0.04	7.77 ± 0.10	6.17 ± 0.28
% TBO	9.77 ± 0.38	5.79 ± 0.19	13.30 ± 0.12	6.81 ± 0.21	5.43 ± 0.32

potential (TBP).

The (Coulomb-)Morse potential (Eq. (1)) allows describing the interactions between an oxide ion (O^{2-}) and a generic cation (M^{n+}, both a former or a modifier) or between two oxide ions and it is composed of three contributions:

$$U^{C-M}(r_{ij}) = \frac{Z_i Z_j}{r_{ij}} e^2 + D_{ij}\left[\left(1 - e^{-a_{ij}\left(r_{ij} - r_{ij}^0\right)}\right)^2 - 1\right] + \frac{C_{ij}}{r_{ij}^{12}} \quad (1)$$

The first term describes the long-range Coulombic interactions and includes the charges (partial and fixed) of the i th and j-th ions, the distance between them (r_{ij}), and the elemental charge *e*. The second term represents the Morse potential and includes three parameters: D_{ij} is the energy of the system at the equilibrium distance, a_{ij} is correlated to the curvature and r_{ij}^0 is the equilibrium distance. The third and last term represents a repulsive contribution, and it is useful to avoid a collapse of atoms at high-temperature and high-pressure systems.

The Buckingham potential is the second functional form (Eq. (2)) and it is used to describe the repulsive interactions between former ions (T-T interactions):

$$U^{B}(r_{ij}) = A_{ij} \cdot e^{\left(-\frac{r_{ij}}{\rho_{ij}}\right)} \quad (2)$$

The parameters A_{ij} and ρ_{ij} describe the repulsions.

Finally, to describe the Si-O-Si three-bodies interactions a screened harmonic function (Eq. (3)) is used:

$$U^{TBP-Screened}(\theta_{ijk}) = \frac{K_{ijk}}{2} \cdot \left(\theta_{ijk} - \theta_{ijk}^0\right)^2 \cdot e^{-\left(\frac{r_{ij}}{\rho} + \frac{r_{jk}}{\rho}\right)} \quad (3)$$

Where θ_{ijk}^0 is the reference angle between atoms i,j and k, K_{ijk} is the force constant and ρ is a decaying parameter.

2.1.2. PMMCS potential [7]

PMMCS potential was developed in 2006 and its functional form encloses only two body interactions as reported in Eq. (1). This Force Field is the precursor of the BMP FFs and it lacks the three-body interactions and the repulsion between network cations (that is, Eqs. (2) and (3)); the parameters of the PMMCS potential are reported in Table 2 of the ESI.

2.1.3. SHIK potential [9]

Another important potential is the one that has been developed by Sundararaman, Huang, Ispas, and Kob which is usually referred to as SHIK potential. It uses the rigid ion model and a Buckingham potential for all the ions' pair interactions. Differently from the previously described potentials, the SHIK potential uses variable charges: cationic (partial) charges are calculated to take into account the polarization effects on the ions themselves, and for this reason, there are some differences with the formal charges. The charge of oxygen is calculated as the last one to maintain the electroneutrality of the system, and for this reason, it changes with the composition.

Table 4
Na and Ca coordination numbers in albite and anorthite glasses. The radial cutoffs used for Na and Ca are 3.1 Å.

	Albite PMMCS	BMP	SHIK	Du	CS
Average coord. Na-O	6.6 ± 0.3	6.3 ± 0.2	5.1 ± 0.2	6.7 ± 0.2	5.2 ± 0.1
Average coord. Na-BO	5.8 ± 0.2	5.8 ± 0.1	4.5 ± 0.2	5.9 ± 0.2	4.8 ± 0.1
Average coord. Na-NBO	0.8 ± 0.2	0.5 ± 0.1	0.6 ± 0.1	0.8 ± 0.1	0.4 ± 0.1
	Anorthite PMMCS	BMP	SHIK	Du	CS
Average coord. Ca-O	6.6 ± 0.3	6.7 ± 0.2	6.2 ± 0.2	6.8 ± 0.3	5.7 ± 0.2
Average coord. Ca-BO	4.7 ± 0.3	5.5 ± 0.2	4.2 ± 0.2	5.5 ± 0.2	4.7 ± 0.2
Average coord. Ca-NBO	1.9 ± 0.2	1.2 ± 0.1	2.0 ± 0.02	1.3 ± 0.2	1.0 ± 0.1

$$V(r_{ij}) = A_{ij} e^{-B_{ij} r} - \frac{C_{ij}}{r_{ij}^6} + \frac{D_{ij}}{r_{ij}^{24}} + z_i z_j e^2 \left[\frac{1}{r_{ij}} - \frac{1}{r_{cut}^w} + \frac{\left(r_{ij} - r_{cut}^w\right)}{\left(r_{cut}^w\right)^2}\right] \quad (4)$$

The functional form includes a short-range Buckingham potential (complete with both the repulsive and the attractive contributions), a repulsive interaction to avoid that the system collapses at too high pressure and temperature, and a long-range electrostatic interaction computed through the Wolf truncation method [17]. As we can see the electrostatic term has also a truncated component, that depends on the type of interaction being considered (for Coulombic interactions r_{cut}^w = 10 Å, and Van der Waals ones r_{cut}^w = 8 Å). The parameters of the SHIK potential are reported in Table 3 of the ESI.

2.1.4. Du potential [6]

Du potential is based on the original Teter potential and extends it to other components. It is based on the rigid ion model. This potential treats only the two body interactions and its functional form (Eq. (5)) contains two terms, the long-range interactions' electrostatic contribution, and the short-range interactions' Buckingham potential.

$$V(r_{ij}) = \frac{z_i z_j e^2}{4\pi\varepsilon_o r_{ij}} + A_{ij} e^{-B_{ij} r} - \frac{C_{ij}}{r_{ij}^6} \quad (5)$$

The Buckingham potential becomes unphysically attractive when the interatomic distance r_{ij} is too small. To avoid this problem the authors introduced a second functional form (Eq. (6)) which deals exclusively with very short-range interactions. The parameters of the Du potential are reported in Table 4 of the ESI.

$$V(r_{ij}) = \frac{B_{ij}}{r_{ij}^n} + D_{ij} r_{ij}^2 \quad (6)$$

Table 5
Bridges type distribution in albite and anorthite glasses.

%	PMMCS	BMP	SHIK	Du	CS	Random* Distribution
Albite						
Si-O-Si	52.03 ± 0.23	50.68 ± 0.13	54.12 ± 0.34	52.57 ± 0.37	51.97 ± 0.13	56.25
Si-O-Al	41.07 ± 0.19	46.93 ± 0.14	39.38 ± 0.29	40.87 ± 0.32	44.20 ± 0.15	37.50
Al-O-Al	6.99 ± 0.17	2.39 ± 0.06	6.50 ± 0.15	6.56 ± 0.19	3.83 ± 0.05	6.25
Anorthite						
Si-O-Si	18.08 ± 0.25	9.29 ± 0.09	22.67 ± 0.24	19.27 ± 0.29	17.74 ± 0.10	25.00
Si-O-Al	52.10 ± 0.24	76.70 ± 0.11	46.23 ± 0.31	52.48 ± 0.39	57.00 ± 0.19	50.00
Al-O-Al	29.82 ± 0.19	14.01 ± 0.03	31.10 ± 0.08	28.25 ± 0.12	25.26 ± 0.05	25.00

* $\%Si\text{-}O\text{-}Si = x_{Si}^2 \times 100; \%Si\text{-}O\text{-}Al = 2x_{Si}x_{Al} \times 100$; *$\%Al\text{-}O\text{-}Al = x_{Al}^2 \times 100$.

2.1.5. Core-Shell potential [10]

The Core-Shell (CS) potential employs formal ionic charges and the polarizability of the anions (in this study oxygen anions) is handled by dividing the total negative charge Z into two parts: one massive core with charge Z-Y and a massless shell with charge Y. Nucleus (core) and electronic cloud (shell) are connected by a spring with a harmonic potential like:

$$V(r_{ij}) = \frac{1}{2}k_{CS}r_{ij}^2 \tag{7}$$

Short-range forces act only between the oxygen shells and cationic cores and oxygen shells while long-range forces act also between the cores. The functional form of this potential (Eq. (7)) includes a Buckingham potential and a Coulomb potential for the two body interactions and a harmonic potential for the three body interactions.

$$V(r_{ij}) = A_{ij}e^{-B_{ij}r} - \frac{C_{ij}}{r_{ij}^6} + \frac{z_i z_j e^2}{r_{ij}} + \frac{1}{2}k(\theta - \theta_0)^2 \tag{8}$$

The Core-Shell potential parameters are reported in Table 5 of the ESI.

2.2. Structural models: crystals and glasses

The structures of albite and anorthite crystals were taken from literature [11,12].

The two glass structures have been generated by randomly placing the atoms in a cubic box (whose side is related to the experimental density of the glass) and then applying the traditional melt-quench approach by MD simulations [3] using the DL_Poly® code [18]. In this process, the initial system is heated at a high temperature to generate a melt; then it is rapidly cooled down under the glass transition temperature, to generate the amorphous system. The quenching was simulated both in NVT and in NPT ensembles [19,20]. At first the system is kept at 2500 K for 40 ps to completely melt the starting structure. Then it is cooled down to 300 K with a monotone cooling rate of 5 K/ps and finally it is kept at 300 K for 200 ps to equilibrate the system. At the end of the last step, the trajectory of the system is extracted and analyzed.

As for the rigid ionic models, the motion integration is carried out using the Verlet-Leapfrog algorithm with a time-step of 2 fs. Instead, a time step of 0.2 fs is used to decouple the core and shell motion. No energy drifting have been observed during simulations.

The coulomb interactions were calculated by the Ewald summation method (precision 1E-5) except for the SHIK potential. The cutoff distance is 12 Å for the BMP, PMMCS, Du, and CS potentials, and 10 Å for the SHIK potential. The short-range interactions were evaluated using cutoff values of 7.0 Å for BMP and CS, 8.0 Å for SHIK, and 5.5 Å for PMMCS.

Concerning the NPT simulations, it has been observed that for some initial configurations, the box undergoes a kind of explosion due to strong repulsive interactions that stop the execution. For this reason, all the NPT simulations are preceded by an NVT high-Temperature step. The employed thermostat and barostat are the Berendsen ones, with frictional constants set to 0.2 ps.

2.3. Simulated properties

2.3.1. Pair distribution functions

The Pair Distribution Function (PDF) represents the probability density of encountering a j-th atom at a distance r from the central atom i-th [8]. It is important to describe the local structure of the system and from its analysis, we obtain the most probable distance for a pair of atoms and the average distance between two atoms. The PDF is calculated following this ratio:

$$\rho_{ij}(r) = \frac{\sum_{k=1}^{M} N_j^k(r, \Delta r)}{M\frac{1}{2}N_i\rho_j^0 V(r, \Delta r)} \tag{9}$$

Where N_j^k is the number of the encountered atoms j in the k-configuration, N_i is the total number of the i-th atoms, V is the space volume included in the sphere of thickness Δr, M is the number of the k sampled configurations and ρ_j^0 is the total density of j-th atoms. The average bond distances have been computed by following the procedure reported in ref [21].

2.3.2. Coordination number

The number of the *j*-th atoms which surround a central *i* th atom in a defined distance between two positions r_A and r_B of the space is given by an integral of the radial distribution function $g_{ij}(R)$:

$$CN_{ij}(r_A, r_B) = \rho_j^0 \int_{r_A}^{r_B} g_{ij}(r)dr \tag{10}$$

2.3.3. Thermal expansion coefficient

The Linear-Coefficient of Thermal expansion (CTE) is defined as:

$$\alpha(T) = \frac{1}{l_0}\left(\frac{\partial l}{\partial T}\right)_p \tag{11}$$

Where l is the length of the cell size at temperature T and l_0 is the length of the cell at 300 K. To obtain the CTE, $\alpha(T)$, we warmed the system from 300 K to 2000 K with a heating rate of 5 K/ps using the NPT ensemble. The change in the cell side has been recorded and the CTE computed by fitting Eq. (11) in the temperature range from 300 to 400 K

2.3.4. Elastic moduli

The Young Modulus (E) describes the resistance of a rigid body to uniaxial load. In this work, Young's moduli of the investigated glasses have been determined from the stress/strain (σ/ε) diagram, which has been obtained by subjecting the samples to uniaxial tensile loading through a gradual elongation with a strain rate $\dot{\varepsilon} = 10^9 s^{-1}$ according to the procedure described by Pedone et al. [22] The deformation has been applied on the three principal axes and the data have been averaged at the end of simulations. The obtained curves have been fitted with a third-grade polynomial which reproduces the non-linear stress/strain behavior ($R^2 > 0.99$) within a strain of 0.15:

$$E(\varepsilon) = E_0\varepsilon + E_1\left(\frac{\varepsilon^2}{2!}\right) + E_2\left(\frac{\varepsilon^3}{3!}\right) + E_3 \tag{12}$$

where E_0 is Young's Modulus at zero strain.

The Bulk Modulus (B) of glass systems, which describes the resistance of the system to compression has been determined by applying hydrostatic pressure to the simulation box and increasing it from 0 to

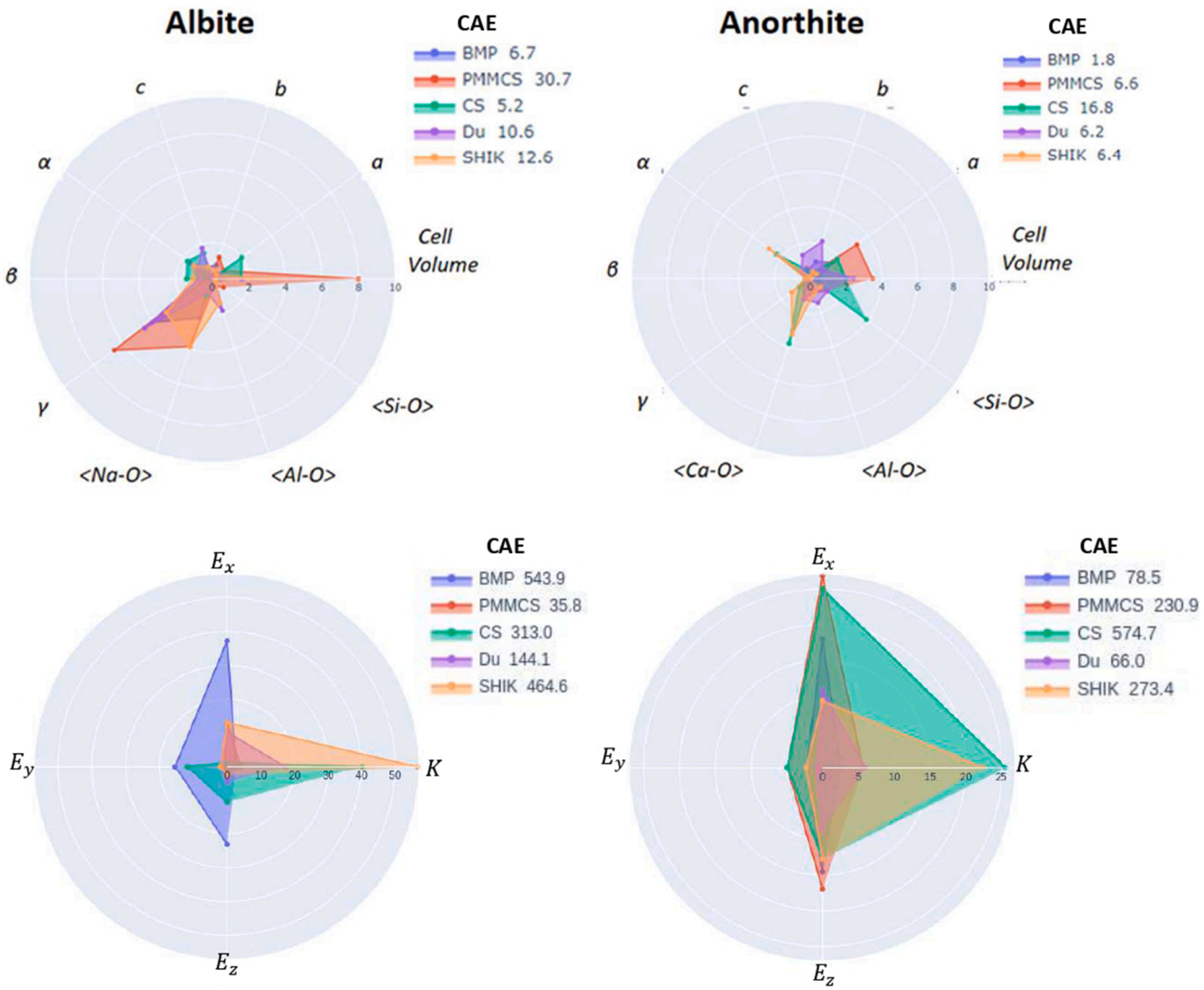

Fig. 1. Star Plots reporting (up) the relative errors on the cell parameters (a, b, c, α, β, γ), cell volume, and average bond distances (Na-O, Ca-O, Al-O, and Si-O), and (low) the relative errors on Elastic Moduli (Bulk Modulus, Young modulus on x, Young Modulus on y and Young Modulus on z) for albite and anorthite crystals obtained with BMP, PMMCS, CS, Du and SHIK potentials. The FFs enclosing the smaller area provide lower errors.

100 kbar with a pressure augmentation rate of 5 kbar/ps and exploiting the relation:

$$B = \rho_0 \frac{\partial p}{\partial \rho} \tag{13}$$

where ρ_0 is the initial density of the glass.

As for the computation of the elastic constants and bulk modulus of the albite and anorthite crystals, we have used the static approach that incorporates a geometry optimization at constant pressure (0 K) and the calculation of the stiffness matrix as described in ref [4].

2.3.5. Density as a function of temperature

To simulate the density as a function of temperature the simulations started from the crystal structure. The first step is to equilibrate the system at 300 K for 25,000 steps in NVT ensemble followed by a NPT run in which the system is heated up from 300 K to 4000 K in 370,000 steps, to obtain a molten phase. The third step is to equilibrate the melt at 4000 K for 100,000 steps. Afterwards, the system is cooled down from 4000 K to 300 K in 370,000 steps and then equilibrated at 300 K for 100,000 steps.

Table 6
Coefficient of Thermal expansion for albite and anorthite glasses.

	Albite (*10^{-6} K^{-1})	Anorthite (*10^{-6} K^{-1})
BMP	9.50 ± 0.49	8.96 ± 0.28
PMMCS	9.39 ± 0.85	9.47 ± 0.12
SHIK	10.35 ± 3.05	7.38 ± 0.59
Du	8.39 ± 1.55	8.51 ± 0.34
CS	3.84 ± 1.36	4.72 ± 0.37
Exp.	7.40	4.90

Table 7
Elastic Moduli for all the tested FFs.

	Albite		Anorthite	
	B (GPa)	E (GPa)	B (GPa)	E (GPa)
BMP	40.3 ± 0.4	65.6 ± 2.4	66.3 ± 2.4	82.9 ± 0.5
PMMCS	51.0 ± 2.7	75.9 ± 1.4	79.2 ± 0.5	98.8 ± 0.9
SHIK	44.1 ± 5.1	65.1 ± 1.7	75.6 ± 2.4	83.9 ± 1.9
Du	44.9 ± 2.3	74.1 ± 2.8	68.3 ± 2.4	86.6 ± 3.3
Core Shell	82.7 ± 2.9	91.8 ± 2.9	103.1 ± 2.6	105.8 ± 3.1
Exp.	38.6	71	69.3	96.2

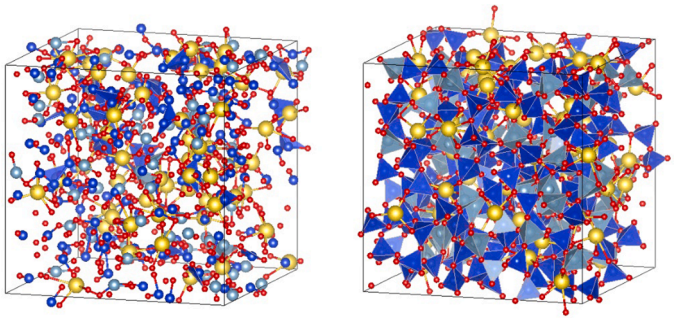

Fig. 2. Albite: starting cell with randomly placed atoms (left) and final cell after the melt-quench protocol containing the BMP interactions (right).

3. Results

3.1. Albite and anorthite crystals

Fig. 1 reports (up) the star plots with the relative error on the cell parameters, volume, and average distances and (low) the Elastic Moduli for albite and anorthite crystals obtained with the tested potentials. All the numerical values are reported in Tables 6 and 7 of the ESI.

As for the cell parameters of the albite crystal, BMP and CS potentials give more accurate results with Cumulative Absolute Errors (CAEs) of 6.7 and 5.2. Du and SHIK perform well with CAEs of 10.6 and 12.6, respectively. PMMCS provides the larger AEs (30.7) because it underestimates the volume (8%) and the γ angle (6.6%).

As for the average bond distances, the ones computed with BMP are the most accurate, especially those of strong covalent bonds. However, in general, all the FFs give satisfactory results with CAEs $< 4\%$.

It is worth mentioning that for the BMP potentials we have used a cut-off for the three-body potential describing the Si-O-Si interactions of 3.1 instead of 3.3 as used in the original manuscript [8]. This is because the albite crystal has wider Si-O-Si angles of about 151 and 161° which are not well reproduced if the original three-body potential is applied. The three-body interaction that is present in the BMP potential gives a prediction of smaller Si-O-Si angles with respect to experimental values. For the angles, the most accurate potential is CS. PMMCS correctly simulates mechanical properties.

All FFs give the same trend for the Young Modulus components; the one that better reproduces Elastic moduli is Du potential, while the remaining four overestimate these values with CAEs higher than 100.

Regarding anorthite, all the FFs give satisfactory results with CAE of 1.8, 6.6, 16.8, 6.2, and 6.4 for BMP, PMMCS, CS, Du, and SHIK potentials, respectively.

SHIK and BMP potentials provide more accurate results on cell parameters. Regarding the average bond distances, BMP seems to give better predictions (relative error < 0.02). As happened for albite crystal, CS gives good results for bond angles. PMMCS does not reproduce accurately the elastic moduli properties of anorthite. BMP and Du potentials show better results with respect to PMMCS while SHIK predicts $E_y > E_z$ (inverted trend).

3.2. Albite and anorthite glasses

In this section, we report the structural analysis carried out on the albite and anorthite glass structures obtained through MD simulations.

Table 3 reports the glass composition in mol% of the constituting oxides as well as the number of the atomic species in the simulation box and the experimental density [15]. Fig. 2 shows the starting and final configurations for the albite system before and after the melt-quench.

3.2.1. Short range order (SRO)

3.2.1.1. Network formers. Fig. 3 reports the PDFs for Si-O and Al-O pairs in the two glasses obtained with the different FFs. From the PDF, information such as the most probable bond distances (the maximum of the function), the average bond distances and coordination numbers can be extracted.

Firstly, we can observe two distinct behaviors that involve on one side the BMP and PMMCS potentials and on the other side SHIK and Du potentials. Indeed, all the PDFs of BMP and PMMCS are similar one to the other and tend to show wider peaks than SHIK and Du ones. CS seems to have intermediate behavior.

The vertical lines inserted in the graphs represent the bond distances Si-O (1.62 Å) and Al-O (1.74 Å) of crystal structures. Those parameters are not comparable with bond distances in the amorphous glass but can

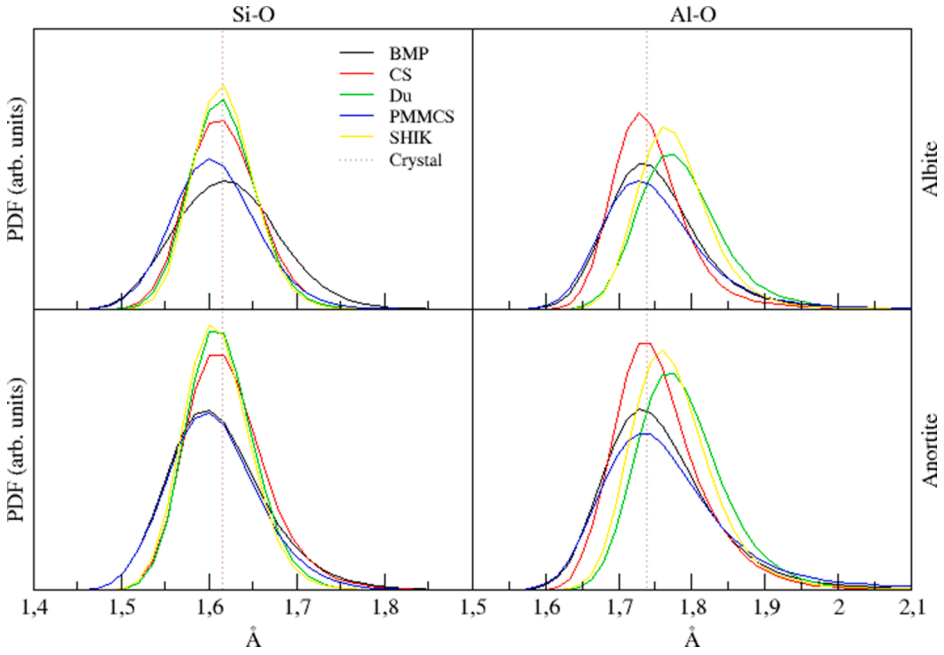

Fig. 3. Comparison between the Si-O and Al-O PDFs computed using the five potentials.

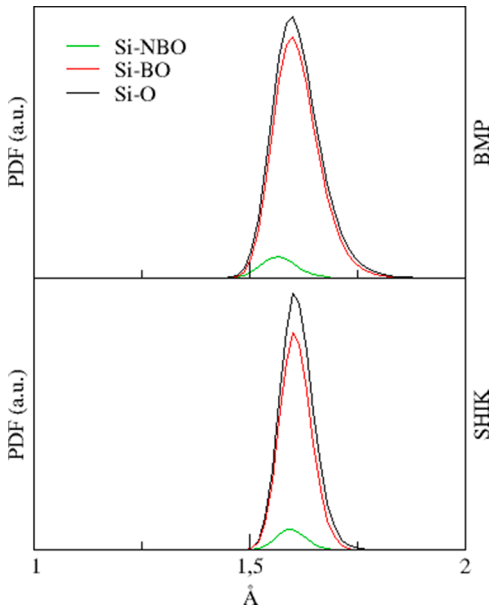

Fig. 4. PDF of Si-O interaction with NBO/BO contributions in anorthite.

be useful as a reference. Concerning the Si-O bond in albite, all the PDFs show the maximum value in correspondence with the bond distance of the crystal (1.62 Å), with exception of PMMCS (1.60 Å). On the other hand, for Anorthite, SHIK, Du and CS have the maximum distance at 1.61 Å, PMMCS and BMP at 1.60 Å. All the potentials provide Si-O distances in good agreement among each other and with experimental data on silicates [23–26]

It is interesting to note that the differences between the SiO PDFs observed for the PMMCS and BMP potentials do not appear in anorthite ones, here the two curves are perfectly overlapped. The PDFs obtained with the BMP potential are wider than the one of PMMCS: this indicates a higher variability of the local geometry. This is due to the significant amount of Si-O-Si bonds (see next section) present in albite glasses and on which the three-body potential is applied for the BMP. Instead, in anorthite Si-O-Si bonds are barely present, and the Al-O-Si bridges dominate, for which the three-body potential does not apply.

As long as it concerns the Al-O bond, similar considerations both for albite and anorthite glasses can be done. BMP, PMMCS, and CS potentials show maxima at the typical crystal distances (1.74 Å), while SHIK and Du ones tend to give higher values (1.76 Å and 1.77 Å, respectively) but with smaller peaks.

Beyond the mere analysis of the quantitative results, the bond distances found are perfectly in agreement with the range of values from other aluminosilicate glasses with the same modifier species [27].

The T-O curve (where T = Si, Al) is the convolution of T-BO and T-NBO components. As an example, the explicit PDF of BMP and PMMCS are reported for anorthite glass in Fig. 4.

3.2.1.1.1. Bond angle distribution (BAD). Fig. 5 reports the O-Si-O and O-Al-O BADs for albite and anorthite glasses obtained with the different FFs.

The figure shows that all the FFs describe similar intratetrahedal geometry. In both glasses, the maximum of the BAD corresponds to angles between 108°−109° for O-Si-O and 105°−108° for O-Al-O: these values are smaller than the theoretical tetrahedron value (109.47°). CS provides narrower BADs denoting more ordered tetrahedral (this is particularly evident for the O-Al-O angle). This is a consequence of the inclusion of three-body potentials on the O-Al/Si-O angles that enforces the tetrahedral coordination of these atoms (without this interaction we would obtain excessive quantities of fivefold coordinate Al and Si).

3.2.1.1.2. Coordination numbers. The coordination number of Si and Al for albite and anorthite glasses, obtained by integrating the radial distribution function up to the first minimum, are reported in Table 2.

All the FFs are in good agreement to describe the coordination sphere of Si and Al cations, particularly for Silicon. As has been shown before [28], the fast cooling rates used, results in the presence of some under or over-coordinated aluminum species. Du and BMP potentials are the ones that simulate the highest presence of Al three-coordinated (8.15 and 5.94%) in albite glass while SHIK the lowest (1.85%). On the other hand, SHIK and PMMCS simulate the highest presence of Al five-coordinated both in albite (0.53 and 0.84%) and anorthite (3.97% and 3.55%) glasses.

3.2.1.2. Network modifiers. The network modifiers of albite and

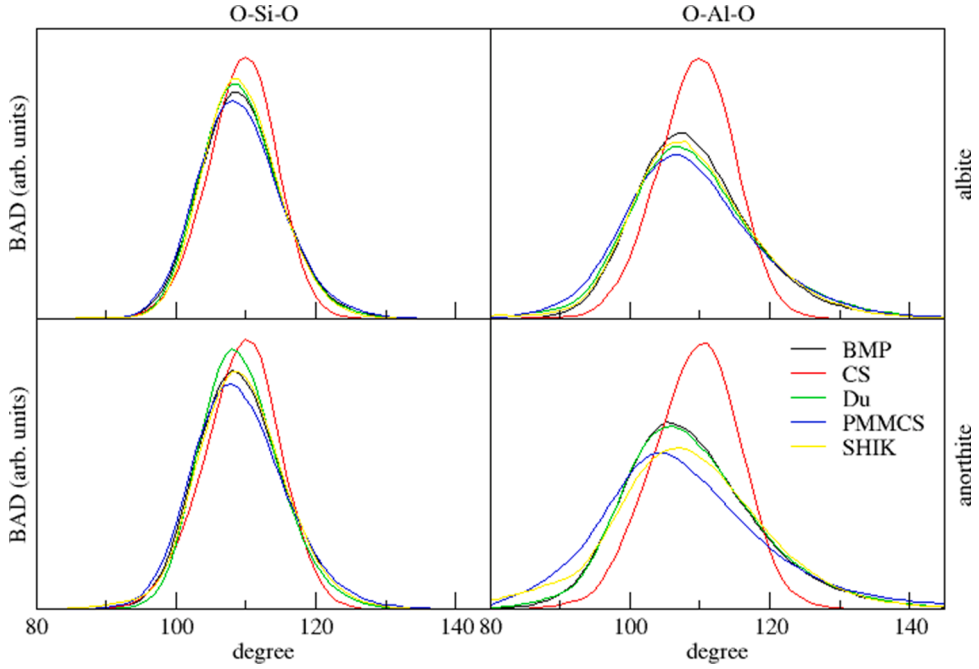

Fig. 5. Comparison between the five potentials simulated BAD for the O-T-O angles.

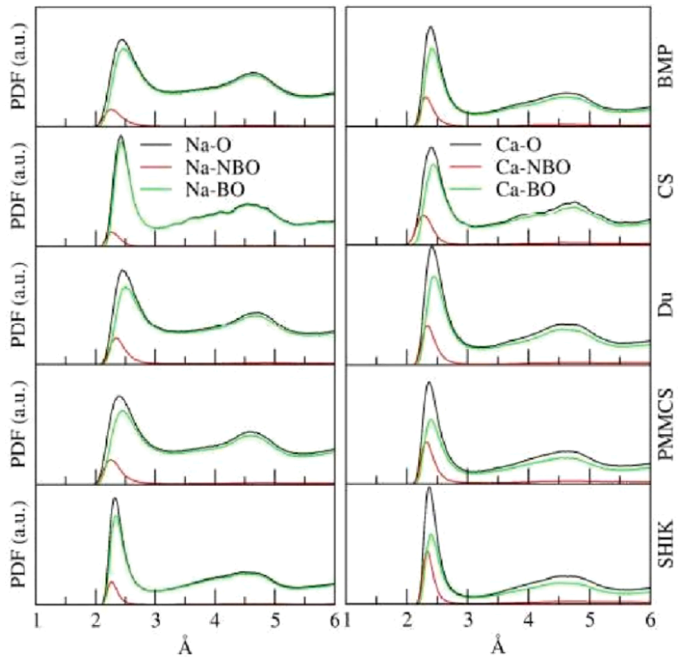

Fig. 6. – Na-O and Ca-O PDFs for albite (left) and anorthite (right) glasses.

anorthite are, respectively sodium and calcium. Differently from former cations, those are mainly related to the lattice's oxygens through electrostatic interactions. The study, also in this case, has been focused on the first coordination sphere and on the bond distances M-O (where M is Na or Ca).

3.2.1.2.1. Oxygen speciation. Na and Ca oxides in glass structures can act as network modifiers by fragmenting the network and forming NBO atoms or as charge compensators of the $[AlO_4]^-$ units.

The given compositions allow the formulation of the following hypothesis:

- In albite glass ($12.5\%Na_2O{\cdot}12.5\%Al_2O_3{\cdot}75\%SiO_2$), each Sodium atom should behave like a charge compensator for an aluminum atom without NBO formation (with stoichiometry Al: Na = 1: 1).
- In anorthite glass ($25\%CaO{\cdot}25\%Al_2O_3{\cdot}50\%SiO_2$), each calcium atom should behave like a charge compensator for two aluminum atoms without NBO formation (with stoichiometry Al: Ca = 2: 1).

However, experimentally there may be the fragmentation of the lattice with the formation of small amount of NBO species [29]. Despite this, the FF that will show the higher percentage of BOs in the two systems should provide the best prediction. The oxygen speciation distributions in albite and anorthite are reported in Table 3.

TBO are the tri-bridging oxygens, that is, oxygen atoms bonded to three former atoms of the network.

All FFs reproduce a fraction of BOs higher than 90% in albite and 75% in anorthite. In particular, the best potentials to simulate the oxygen speciation are CS (with BO: 96.37% for albite and 88.39% for anorthite) and BMP (with BO: 94.85% for albite and 87.00% for anorthite).

As observed in other works [30,31], the high field strength of Ca ions creates more NBOs on anorthite glass. In particular, the albite glass has 97.50% of NBO on Silicon, and only 2.50% on Aluminium as we expected for the negative charge associated with the $[AlO_4]^-$ tetrahedrons. A different situation is the one of anorthite glass where 77.30% of NBOs are on Silicon and 22.70% on Aluminium. These fractions depend both on the different field strengths of Ca ions (with respect to Na ones) and on the different compositions (anorthite has twice the number of Al atoms than albite).

3.2.1.2.2. Pair distribution function. For the albite glass (Fig. 6, left side) we have observed average Na-O distances between 2.40 Å (SHIK) and 2.55 Å (BMP). SHIK and CS potentials show narrower peaks denoting a more ordered environment whereas PMMCS, Du, and BMP potentials provide broader peaks. All the FFs are in good agreement to describe the Na-O bond distances in the range found in experiments [32]. The separation between the bonding and non-bonding components highlights that all the potentials, mainly CS, provide for a higher contribution of the Na-O bond.

For the anorthite glass (Fig. 6, right side) we have observed average Ca-O distances between 2.39 Å (SHIK) and 2.61 Å (BMP). Some differences between the FFs are manifested by examining the different Ca-NBO and Ca-BO components. In particular, the potentials that predict a greater contribution to the Ca-BO curve are BMP, CS, and Du, for SHIK and PMMCS the two functions are similar, and the relative portion of Calcium ions bonded to Non-Bridged Oxygen atoms is considerable.

In anorthite, Ca-O distances range between 2.29–2.89 Å with an average value of 2.49 Å [32]. Therefore, MD simulations are in nice agreement with these data.

3.2.1.2.3. Coordination numbers. The coordination numbers for Na and Ca in albite and anorthite glasses are reported in Table 4:

The coordination numbers of sodium ions in albite glass extracted from MD simulations range from about 5 for SHIK and CS to 6 for BMP to 6/7 for PMMCS and Du potentials. EXAFS measurements indicate 5–6 oxygen neighbors around Na but an exact determination of the coordination is difficult since Na sites are statically disordered and irregular [33]. XANES spectra of sodium aluminosilicate glasses also indicate a distorted 6 coordination environment for Na [32].

Regarding Ca in anorthite glasses, almost 7 oxygens are found in its coordination environment with the PMMCS, BMP, and Du potentials whereas a 6-fold coordination is found with SHIK and CS potentials. All these data are in nice agreement with XANES and diffraction experiments in which a 6–7 coordination is usually found [32,34].

The examination of the coordination numbers of the modifying cations confirms what could be deduced from the radial distribution functions: in the anorthite glass, the PMMCS and SHIK potentials expect a higher amount of NBO oxygen atoms in the proximity of Ca ions with respect to all the other FFs. In albite glass, on the other hand, the presence of BO atoms in the coordination sphere of sodium prevails for all potentials.

3.2.2. Middle range order (MRO)

The study of MRO in glasses is based on the determination of the interconnection of the SiO_4 and AlO_4^- tetrahedral units, the degree of polymerization of the vitreous structure, the bond angles distributions of inter-units and the determination of the oxygen speciation.

3.2.2.1. Bridges type distribution. The Bridges type distribution (BTD) quantifies the percentage of bridges Si-O-Si, Si-O-Al, and Al-O-Al in the glass structure and it is thus a measure of the intermixing between network former cations.

Based on the composition in oxides of the two glasses (albite glass: $12.5\%NaO{\cdot}12.5\%Al_2O_3{\cdot}75\%SiO_2$ and anorthite glass: $25\%NaO{\cdot}25\%Al_2O_3{\cdot}50\%SiO_2$) it is assumed that in the anorthite structure, there is a higher distribution of bridges that contain Al than in the albite one.

Lowenstein's rule (also denoted as Al avoidance rule) states that the Al-O-Si bond is thermodynamically more stable and favored than the Si-O-Si one and it excludes the presence of Al-O-Al bridges into the structure, except for Si/Al ratio lower than 1.

Although, experimentally, this type of link has also been observed for several compositions [35,36], the FF producing the higher percentage of Al-O-Si bridges within the two glass systems (as well as the lower percentage of Al-O-Al bonds) will provide the best prediction.

The bridge type distribution in the albite and anorthite glasses is reported in Table 5. Table 5 also reports the number of bridges that

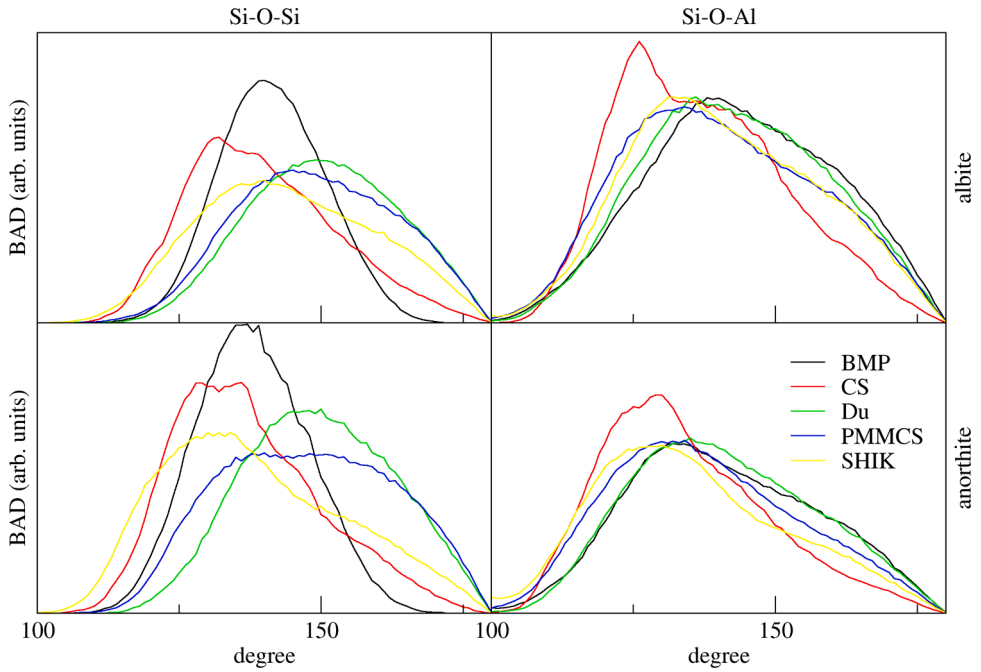

Fig. 7. BAD for T-O-T angles (T= Si, Al) for albite and anorthite obtained with all FFs.

would be generated if Al and Si would distribute randomly around the BOs.

For albite glass, the results are similar to each other for all the listed potentials: more than a half of the bridges are of Si-O-Si type; about the Si-O-Al ones, their amount goes from 39.38% (SHIK) to 46.93% (BMP); the amount of the Al-O-Al bridges goes from 2.39% (BMP) to 6.99% (PMMCS). In general, all FFs lead to generating preferentially Si-O-Al bonds concerning a random distribution of Al and Si around BOs (the % of Si-O-Al bonds would be 37.5%). SHIK provides a lower number of these bonds and Al/Si distributions are more similar to the random one. This probably reflects the similarity of the Si-O and Al-O bond strength for this potential.

As for the Al-O-Al bonds, PMMCS, SHIK, and Du potentials provides a number of such bonds similar to a random distribution (6.25%) whereas BMP and CS provide lower values (2.39 and 3.83%, respectively).

In addition to Lowenstein's rule [37], the following consideration can be expressed: since we observe Al-O-Al bridges only when two tetrahedral units $[AlO_4]^-$ are joined together, a low fraction of this type of bond indicates a more homogeneous dispersion of these units within the structure, avoiding areas with a higher concentration of aluminum than to others.

The composition of anorthite glass is characterized by a relatively higher percentage of aluminum oxide (half of the silicon oxide one). Based on the composition, if Si and Al would be randomly distributed around BOs, we would have 25% of Si-O-Si, 50% of Si-O-Al, and 25% of Al-O-Al.

MD simulations provide a lower number of Si-O-Si bridges (from 9.29% of BMP to 22.67% of SHIK) and higher fractions of Si-O-Al bonds (from 46.23% of SHIK and 76.7% of BMP). The number of Al-O-Al bridges is higher too: BMP predicts a more homogeneous distribution of aluminum within the glass structure with respect to other potentials (it yields 14.01% of Al-O-Al while for the others this value is higher than 25%). It is interesting to notice that all FFs predict a percentage of Al-O-Al bridges that is higher than the percentage of Si-O-Si bridges and higher than the one obtained considering a random distribution of Al ions around BOs. This is due to the presence of calcium that can compensate for two negative charges beard by two connected AlO_4 units.

3.2.2.2. Intertetrahedral bond angle distribution. T-O-T (where T = Al or Si) angles have a relevant role in the study of the middle-range order because they give further information about the interconnection between tetrahedral units in the network.

The Si-O-Si and Si-O-Al BADs for albite and anorthite obtained using the different FFs are reported in Fig. 8. We have not reported the Al-O-Al BADs because of their low amount in the glasses.

For both albite and anorthite glasses, the FFs provide similar average Si-O-Al bond angles. As for the albite glass, the maxima are included in the range of 131°–140°; the only exception is CS which produces an average angle of 126° As for anorthite glass, all the maxima values vary between 127° and 135°. Aside from the CS, whose peak is better defined; all functions have very broad bands.

The Si-O-Si bond shows, on the other hand, very different distribution curves for the different potentials. As for albite, BMP finds out its maximum at 139.5°, CS at 132°, Du at 149.5°, PMMCS at 145° and SHIK at 140° For anorthite, there are maxima at 135.5° for BMP, 129° for CS, 147.5° for Du, 145.5° for PMMCS, and 132.5° for SHIK.

It is in the analysis of bond angles T-O-T that the BMP's TBP of Si-O-Si interaction stands out. If the distributions of the Si-O-Al bond computed with the BMP and PMMCS FFs are almost overlapping (since the aforementioned interaction is absent, the functional forms are the same), the same cannot be said for the Si-O-Si bond. In this last case, for both glasses, the BMP distribution turns out to be tighter and shows its maxima at lower bond angles concerning PMMCS. This explains the fact that the TBP interaction prevents a disproportionate enlargement of former oxygen-former bridges and allows obtaining a more regular distribution of the bond angles.

3.2.2.3. Q^n species distributions. The distribution of the Q^n species gives information on the degree of polymerization of the glass structure. Since modifying oxides fragment the constituted silicate network, they are usually the cause of the presence of NBO oxygen atoms inside the network. Being the composition of anorthite glass characterized by a greater quantity of modifier oxide with respect to albite glass (25% of CaO against 12.5% of Na_2O), we expect to find a higher distribution of Q^n species with $n < 4$.

However, since for tetrahedral units $[AlO_4]^-$ modifying oxides should act only from charge compensators, the best prediction will be

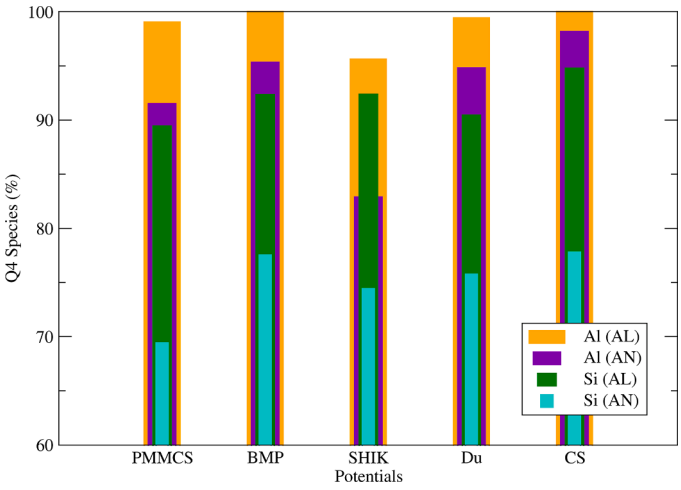

Fig. 8. Percentage of Q^4 species in albite (AL) and anorthite (AN) glasses.

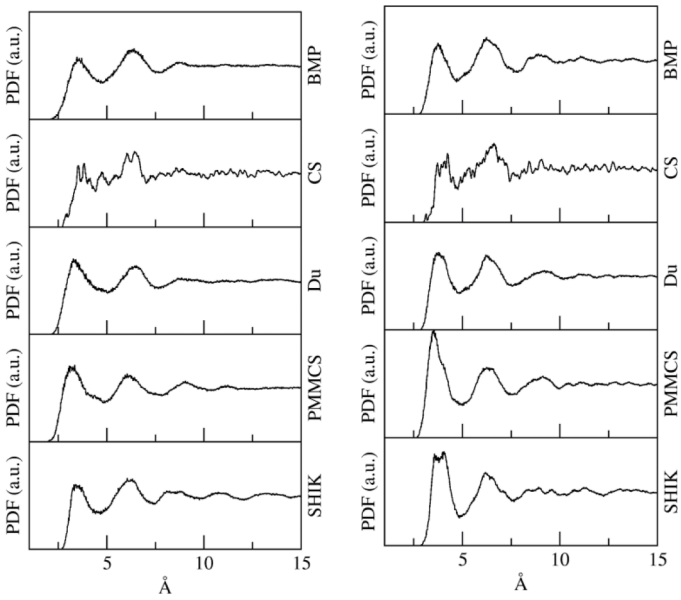

Fig. 9. PDF of Na-Na interaction for albite glass (left) and for Ca-Ca interaction for anorthite glass (right).

provided by the potential which, for both glasses, will show the highest percentage of Q^4 aluminum.

Fig. 8 reports the Q^4 distribution for Si and Al in the albite and anorthite glasses.

The figure reveals that almost all NBOs are connected to Si since Al is almost 100% present as Q^4 species (except for the results obtained with the SHIK potentials). The percentage of silicon Q^3 species ranges between 5.2 and 10.47%.

As for the anorthite glass, we observed a higher amount of NBOs which form Q^2 (1.4–3.6%) species and Q^3 (20–26%) species for silicon. As for albite, SHIK potentials provide a higher amount of Q^3 species (>15%) on Al which is not what one would expect. Indeed, the AlO_4 unit already bears a negative charge and the formation of one NBO should be unfavorable since the unit would bear a greater negative charge.

3.2.2.4. Pair distribution function. For completeness, the modifier-modifier PDFs are reported in Fig. 9. Each relative maximum represents an M-M coordination sphere: more peaks are identifiable; the more structure will be ordered in the medium range.

As for the Na-Na PDF in albite glass, all the FFs show the first maximum for values between 3.4 Å (SHIK) and 3.7 Å (BMP). The bands have some regularity for all potentials and the highs are visible; SHIK is the potential with the greatest number of relative maxima. Three FFs over five (SHIK, CS, BMP) show a second peak more intense than the first one, and this is in agreement with experimental data [34]; for PMMCS and Du the maximum which matches with the first Na-Na interatomic distance has a slightly higher intensity.

As for the Ca-Ca PDFs in anorthite glass, all FFs have three peaks according to experimental data[36]: the first peak is in the range between 3.5 Å (SHIK) and 4 Å (CS), the second between 6.1 Å (SHIK) and 6.6 Å CS, the third at 8.8 Å. PMMCS and SHIK show a very intense peak for the first Ca-Ca interatomic distance, BMP and Du have the same intensity for both the first and the second band, CS provides for a greater intensity of the second maximum with respect to the first one.

As long as it concerns PDFs for Modifier-Al pairs (Na-Al in albite and Ca-Al in anorthite) reported in Fig. 10, we note that the first maximum corresponds to greater distances than for Modifier-Si ones. The Modifier-Al PDFs (on the left) have their first maxima at about 3.20 Å, while the Modifier-Si PDFs (on the right) have their first maxima at about 3.60 Å. This consideration confirms the hypotheses that were supposed at the beginning of this paragraph on Network Modifiers, about the charge compensator role of the two modifier cations in these structures and the consequent formation of NBO species.

3.3. Physical properties of albite and anorthite glasses

3.3.1. Coefficient of thermal expansion

Table 6 reports the coefficient of thermal expansion for both glasses simulated using the investigated FFs as well as the experimental ones [15]. The computed CTE has been extracted by making a linear regression in the range of 300–400 K of the cell length vs temperature diagram for glasses generated using a cooling rate of 5 K/ps. These data have been extracted from simulations performed with simulation boxes of about 10k atoms. The associated errors are the standard deviations of the CTE results for three replicas of each glass.

It is interesting to note that apart from PMMCS, Du and CS potentials, which show an opposite trend to the experimental one, the other two potentials are in agreement to describe the linear thermal expansion coefficients for both glasses. They predict a higher CTE for albite than for anorthite in agreement with experimental evidence. This is a consequence of the more packed structure of anorthite glasses and the stronger energy bond for Ca-O than Na-O. In general, all the computed CTEs are overestimated. As demonstrated in Section 3.4, this is due to the high cooling rates used in computer simulations and to simulation boxes which are too small to investigate this property [38,39]. Anyway, as we can see from the associated errors to CTE values, all the FFs provide similar results, except for CS potential which gives very underestimated values. We chose to perform all the following calculations with BMP because it provides smaller errors to CTEs.

3.3.2. Elastic moduli

The Young's and Bulk moduli of the albite and anorthite glasses simulated with the different FFs are reported in Table 7 together with the experimental values. The errors associated with these data are within 5.0 GPa.

BMP is the potential that provides, on average, elastic moduli for both glasses in better agreement with experimental values with relative errors between 1.5 and 13% for albite and anorthite. As can be seen, the bulk modulus is reproduced well with errors of 4%. The potential that presents the worst data is CS, which makes a relative error higher than 110% in the albite's Bulk Modulus. This is expected since the CS parameters are generally fitted only considering structural properties.

3.3.3. Density

In this section, we investigate the variation of the density of both albite-like and anorthite-like systems as a function of the temperature

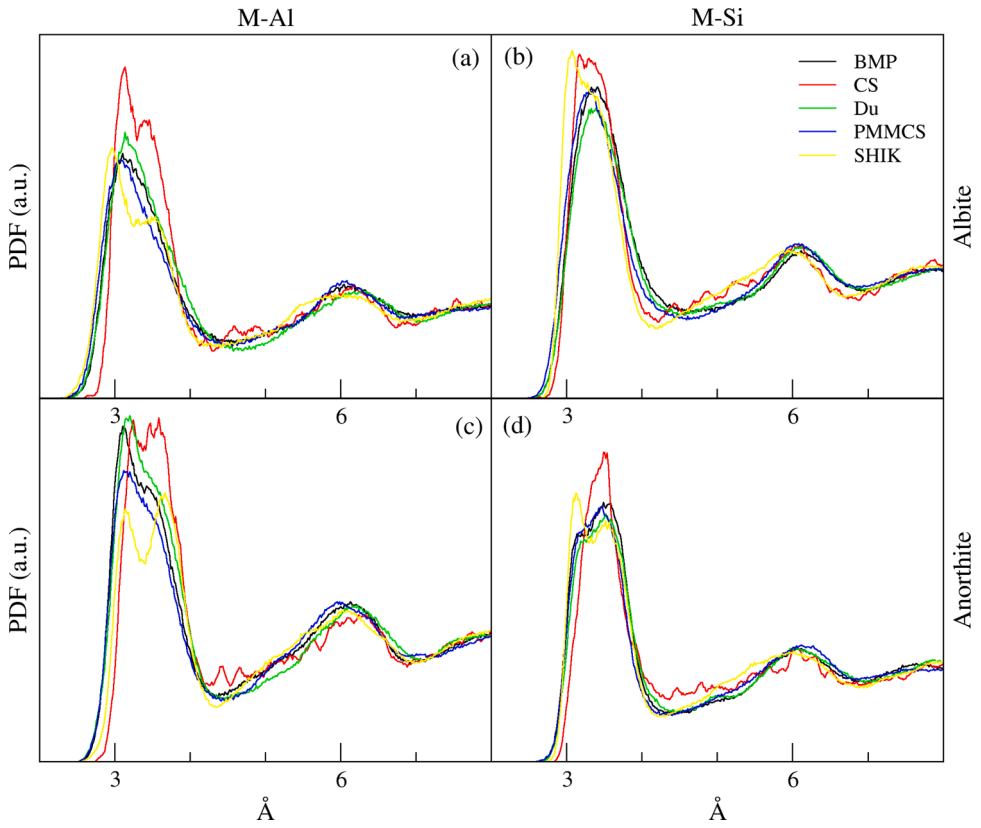

Fig. 10. Comparison between the five potentials of (a) Na-Al PDFs for Albite, (b) Na-Si PDFs for Albite, (c) Ca-Al PDFs for Anorthite, (d) Ca-Si PDFs for Anorthite.

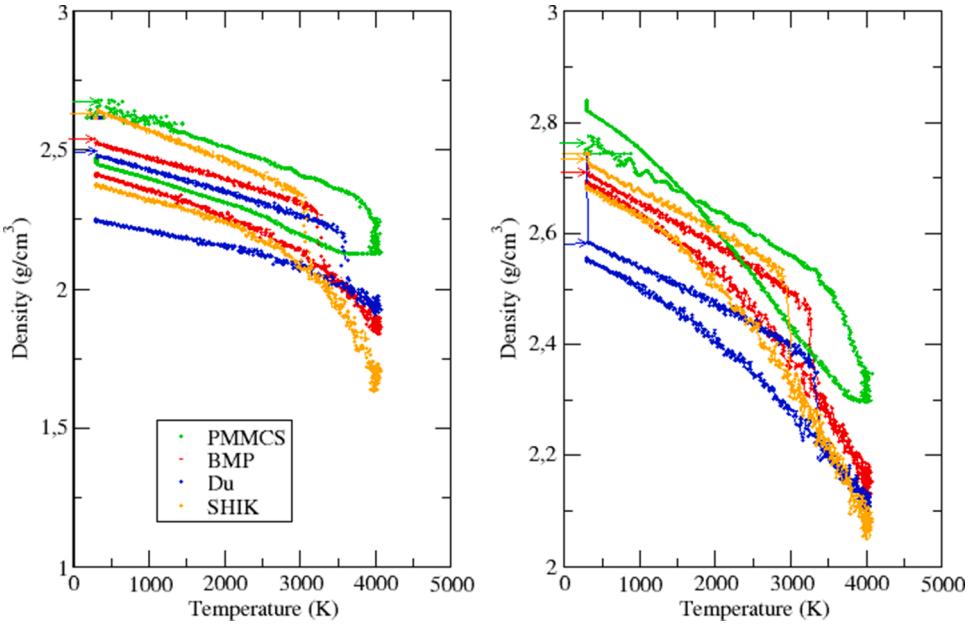

Fig. 11. Density behavior as a function of temperature: from the crystal (arrow), through the molten phase, to the glass for albite (left panel) and anorthite (right).

going from crystals to the melt and then to the glassy state. All the potentials reproduce the expected trend, that is, the density slowly decreases with temperature up to the melting temperature. Then it decreases abruptly because of the phase transition. Finally, the density of the melt slowly and continuously increases during quenching up to the value adopted by the glass. The density of the glass is lower than that of the crystal for all potentials except for the PMMCS potentials which do not reproduce well the density difference between the anorthite glass and crystal.

The left panel of Fig. 11 shows that the SHIK potential is the one which better reproduces the density value for the albite glass (2.37 vs 2.38 g/cm^3), followed by BMP (2.40 g/cm^3), PMMCS (2.46 g/cm^3) and Du (2.25 g/cm^3). The potential which better reproduces the density of the crystal is PMMCS (2.61 vs 2.62 g/cm^3), followed by SHIK (2.64 g/cm^3), BMP (2.54 g/cm^3), and Du (2.47 g/cm^3).

For the anorthite system, the performances on glasses are quite

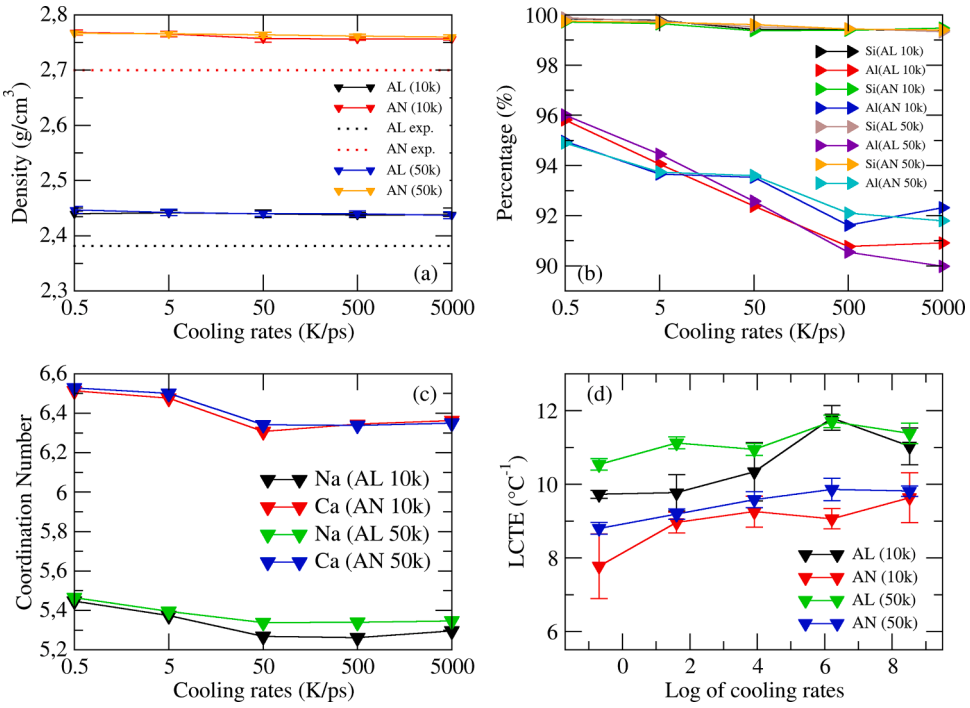

Fig. 12. (a) Density, (b)% of Si and Al 4-fold coordinated, (c) Coordination Number of Na and Ca, (d) CTE for albite and anorthite-like glasses with BMP potential at the five different cooling rates (0.5, 5, 50, 500, 5000 K/ps).

similar to albite ones. This time BMP potential is the best one (2.69 vs 2.70 g/cm^3), followed by SHIK (2.68 g/cm^3), PMMCS (2.82 g/cm^3), and Du (2.56 g/cm^3). The potential that better reproduces the density of anorthite crystal is PMMCS (2.76 vs 2.75 g/cm^3), followed by SHIK (2.73 g/cm^3), BMP (2.72 g/cm^3) and Du (2.58 g/cm^3).

Fig. 11 shows also that the PMMCS produces the melt with higher density whereas SHIK the lower. From the literature, it is known that the density of albite melt, starting from crystals, is 2.32 g/cm^3 at 1200 °C [40] while that of anorthite is 2.55 g/cm^3 at 1600 °C [40]; it is also important to highlight that the two crystals melting temperatures are, respectively 1120 °C and 1553 °C, so these density values belong to the molten phase in its initial stage. Starting to heat from glasses, it can be found that the density of albite melt is 2.2594 g/cm^3 at 1800 °C [41] while that of anorthite is 2.5954 g/cm^3 at 1622 °C [40]

Considering the first couple of density values from the literature, for albite melt the potential that better reproduces this value is PMMCS (2.30 g/ cm^3), followed by SHIK (2.28 g/cm^3), BMP (2.26 g/cm^3), and Du (2.20 g/cm^3). For anorthite the trend is different, and it starts with SHIK (2.48 g/cm^3), followed by BMP (2.26 g/cm^3), PMMCS, and finally Du. On the other hand, the melting temperature varies with the potentials too and the one determined here is the so-called mechanical melting temperature because it is the temperature necessary to produce melting from the bulk of the system. Since melting starts at the surface or defects of materials, the mechanical melting temperature overestimates the experimental one. SHIK provides the lower melting temperature (respectively 3050 K for albite and 3020 K for anorthite) whereas PMMCS the higher (3930 K and 3750 K). For reliable estimation of the melting temperature, the phase coexisting method should be applied that allows the determination of the thermodynamical temperature [42–44] However, this was not the aim of this work and will be treated successively.

For completeness, it must be said that CS potential has not been reported in these plots because the results were unsatisfactory: during the NPT steps the simulation boxes have undergone severe deformations finally leading to the abrupt crash of the simulations.

3.4. The effect of the cooling rate and box dimension on structure and properties

It is well known that glass structure and properties depend on the cooling rate used during their production. This is the consequence of the metastable nature of the glassy state and different cooling rates lead to different states (and thus structures). The timescale spanned in MD simulations (usually of nanoseconds) does not allow the employment of the cooling rate used in experiments. Indeed, the cooling rates used in simulations range between 0.5 to 10 K/ps whereas a typical cooling rate in experiments ranges between 1 and 100 K/s. Consequently, the simulated glasses have a higher fictive temperature resulting in more disordered structures. The effect of the cooling rate on the structure and properties of different glasses has been investigated in several previous works [38,39,45–48] and thus the discussion here will be limited to only a few structural features and properties.

Fig. 12a reports the density of the albite (AL) and anorthite (AN) glasses at different cooling rates (0.5, 5, 50, 500, 5000 K/ps) simulated using the BMP potential and with simulation boxes containing 10k and 50k atoms. As expected and observed in previous works on silicate glasses (except for silica) the density decreases with the cooling rate. Fast-quenched glasses are less compacted than glasses produced with slower cooling rates. On the other hand, density does not depend on the dimension of the simulation boxes. Fig. 12b reports the percentage of the 4-fold coordinated Si and Al ions in AL and AN whereas Fig. 12c reports the coordination number of Na and Ca in AL and AN, respectively. The percentage of 4-fold coordinated Si ions decreases with the cooling rates, but it is less sensitive to the cooling rate with respect to Al coordination. Indeed, the percentage of 4-coordinated Al ions increases from 90 to 95% decreasing the cooling rate from 5000 to 0.5 K/ps. The rest of Al ions are present as 3-coordinated defects. Instead, Fig. 12c shows that the coordination number of Na in AL increases from 5.30 to 5.44 decreasing the cooling rate whereas that of Ca increases from 6.36 to 6.51. In general, with lower cooling rates the structure has more time to relax, and the cations can reach their optimal coordination numbers and produce more packed structures.

Another structural feature affected by the cooling rate is the spatial

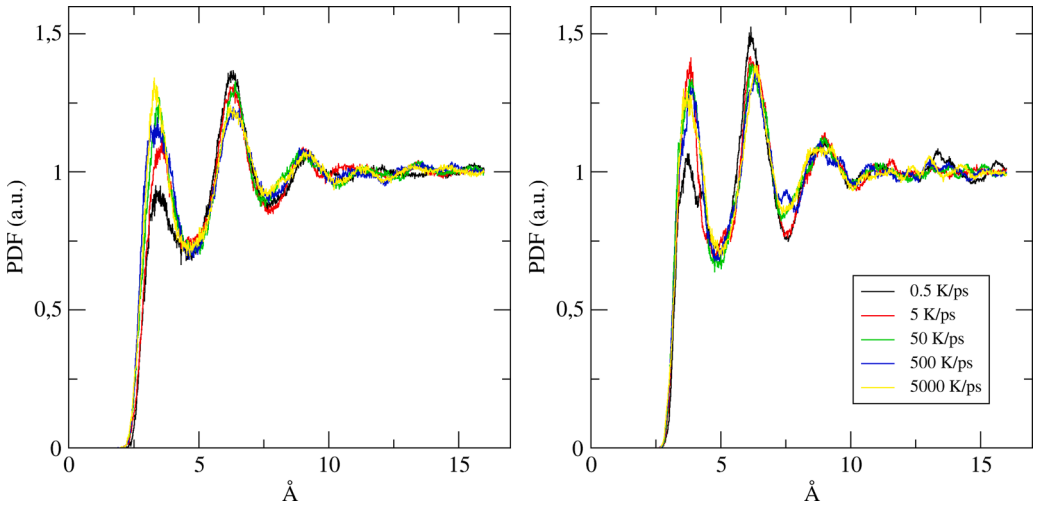

Fig. 13. PDF for Na-Na interactions in albite-like glass (left) and Ca-Ca interactions in anorthite-like glass at the five different cooling rates (0.5, 5, 50, 500 and 5000 K/ps).

distribution of the modifier cations. The Na-Na and Ca-Ca PDF of AL and AN glasses, respectively are reported in Fig. 13. In general, the first peak of both distributions becomes less intense and shifts to slightly longer modifier-modifier distances decreasing the cooling rate whereas the opposite trend is observed for the second peak that describes the correlation between modifiers far apart. The consequence is the increment of the Na-Na and Ca-Ca ordering lowering the cooling rate. This also leads to more packed structures and thus to a higher density.

The different packing of the structures produced using different cooling rates influences the computed CTE as shown in Fig. 12d. Indeed, CTE decreases in a not-monotonic way decreasing the cooling rate. However, it must be emphasized that the computation of the CTE is affected by large errors. The latter reduces with the box dimension. Indeed, the errors found when simulation boxes of 50 thousand atoms are used are 3 times smaller than for 10k atoms (see Fig. 12d). This is due to the metastable nature of glasses (different structures are obtained starting from a different point of the phase space) and the larger fluctuation of the cell in NPT simulations during continuous heating for smaller boxes. The estimated CTEs also depend on the choice of the temperature range on which the CTE is computed.

It is thus important to make at least three replicas for each composition (for all temperatures) and to state the temperature range used to extract the CTE. In this case, the computed CTE refers to a temperature range between 300 and 400 K. As we can see from Fig. 12d, both trends (considering the average values with the associated error) are decreasing as long as the cooling rate decreases. This was expected because with the increase of cooling rate, the glass amorphous structure is more and more disordered and the tendency of atoms to move away from their site becomes greater; thermal history affects structure and properties especially in the middle range order (less in the short-range order structure of the glass) for a decoupling between enthalpy relaxation and volume as long as cooling rate decreases [46].

It is also easy to notice that anorthite CTEs are lower than albite ones: this is experimentally verified (see Table 6), even if for our simulations, anorthite CTEs are double the experimental value. The CTEs of albite are more similar to the experimental value, however, they are overestimated too.

As we can see from Fig. 12d, CTEs computed using boxes with fewer atoms (10k) present the greatest fluctuations (according to statistical physics principles) but they are also those in which the extension of the range of values is greater. This is because, during the heating procedure (which is performed in an NPT ensemble), those systems with a higher number of atoms are those for which the volume increase is larger due to an entropic effect. The logarithmic scale on the x-axis allows us to calculate a linear correlation between the natural logarithm of the heating rate and CTE, both for albite (Eq. (14)) and for anorthite (Eq. (15)).

Table 8
Elastic Moduli for albite and anorthite-like glasses with BMP potential at the five different cooling rates (0.5, 5, 50, 500, 5000 K/ps) on 10k atoms boxes.

	Albite		Anorthite	
	B (GPa)	E (GPa)	B (GPa)	E (GPa)
0.5 K/ps	41.5 ± 0.6	67.6 ± 1.9	69.0 ± 2.3	86.7 ± 2.1
5 K/ps	40.3 ± 0.4	65.6 ± 2.2	66.3 ± 2.4	83.0 ± 0.6
50 K/ps	39.8 ± 0.4	63.6 ± 1.4	63.4 ± 2.1	79.8 ± 1.5
500 K/ps	39.2 ± 0.6	61.8 ± 2.0	60.9 ± 1.9	77.0 ± 1.1
5000 K/ps	38.5 ± 0.8	58.4 ± 2.6	58.2 ± 1.6	74.7 ± 0.8
Exp.	38.6	71	69.3	96.2

$$CTE_{AL}(\ln(v)) = 0.0985\ln(v) + 10.752 \quad (14)$$

$$CTE_{AN}(\ln(v)) = 0.1171\ln(v) + 8.991 \quad (15)$$

Thanks to this empirical law the CTE values for albite and anorthite glasses can be extrapolated at cooling rates similar to the experimental ones (0.5 K/s), resulting in the values of $7.964*10^{-6}{}^{\circ}C^{-1}$ and $5.677*10^{-6}{}^{\circ}C^{-1}$, respectively, which are in very nice agreement with experimental counterparts, $7.4*10^{-6}{}^{\circ}C^{-1}$ and $4.9*10^{-6}{}^{\circ}C^{-1}$, demonstrating that computed glass properties should be extrapolated to obtain values directly comparable with the experimental ones with relative errors lower than 10%. Albeit, this procedure leads to nice results it is quite long and not always possible to follow, especially when several glass compositions must be simulated.

The effect of the cooling rate on the elastic properties has also been investigated using only the simulation boxes containing 10k atoms since this property converges with smaller simulation boxes [49,50]. Table 8 shows that the simulated Elastic Moduli for Albite and Anorthite decrease with the increase of the cooling rate: this is because increasing the cooling rate, the atoms do not have enough time to rearrange in their most stable positions, and it causes a loss in compactness and a decrease in Elastic Properties.

3.5. *The albite-anorthite glass series: physical properties and structure*

After the comparative investigation of the performances of each Force Field on the reproduction of the structure and properties of Albite and Anorthite glasses, we have decided to go into more detail and study

Table 9
Glass compositions: percentage of oxides, number of atoms, density.

	Na_2O%	CaO%	Al_2O_3%	SiO_2%	Na atoms	Ca atoms	Al atoms	Si atoms	O atoms	ρ (g/cm3)
AN	\	25.00	25.00	50.00	\	770	1540	1540	6160	2.70
AL20	2.43	19.32	22.70	55.55	149	593	1393	1705	6167	2.637
AL40	5.05	14.45	20.25	60.35	310	442	1240	1852	6161	2.577
AL60	7.60	9.90	17.40	65.10	468	305	1072	2004	6155	2.495
AL79	10.05	4.80	15.80	69.35	615	147	967	2123	6151	2.438
AL	12.50	\	12.50	75.00	769	\	769	2308	6154	2.38

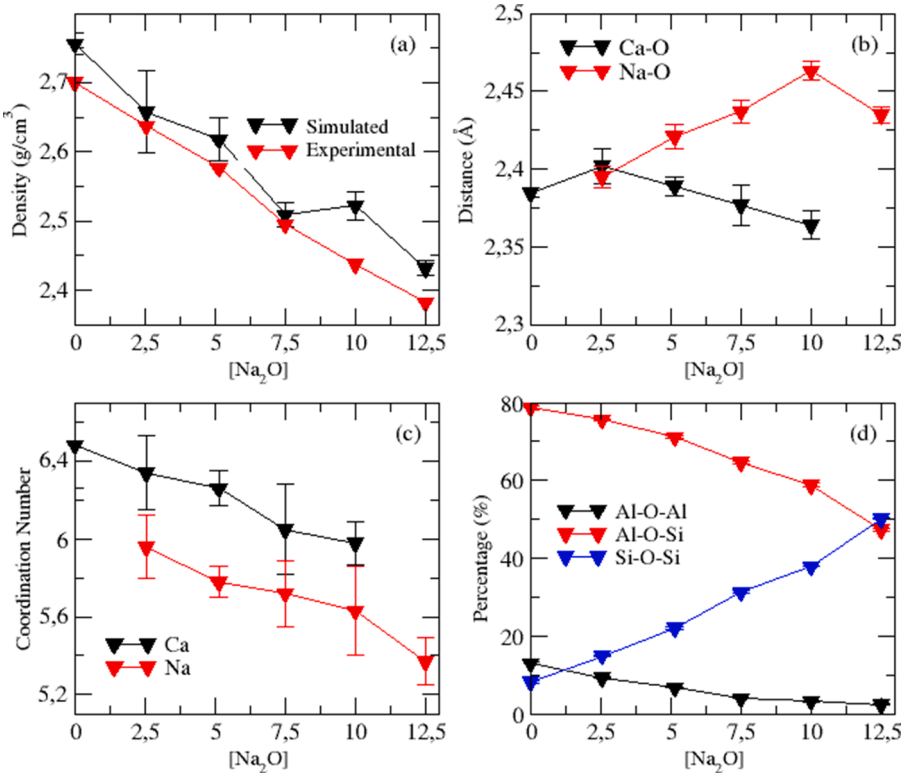

Fig. 14. (a) density, (b) Na/Ca-O bond distances, (c) Na and Ca coordination number, (d) percentage of Si-O-Si, Si-O-Al and Al-O-Al bridge sas a function of sodium content.

a series of plagioclase glasses whose compositional range goes from the albite-like one to the anorthite-like one through four intermediate compositions. Table 9 reports the glass composition in mol% of the constituting oxides as well as the number of the atomic species in the simulation box and the experimental density.

The simulations were done using only BMP potential because of its overall good performance considering all the simulated properties. Moreover, we have decided to perform the melt-quench protocol with a rate of 5 K/ps because this cooling rate provides accurate results in an affordable computational time.

Fig. 14 shows the density, Na/Ca-O bond distances, Na and Ca coordination numbers, and the percentage of Si-O-Si, Si-O-Al, and Al-O-Al bridges as a function of sodium content in the simulated glasses. Going from the anorthite to the albite glass Ca is substituted by Na and Al is replaced by Si. As expected, the density decreases with the addition of sodium oxide and the absolute values are in nice agreement with experimental data. The Na-O distance increases up to the AL79 glass and then decreases whereas the Ca-O distance increases for the AL20 glass and then decreases. Both the coordination numbers of Ca and Na decrease with Ca/Na substitution. The former is from 6.4 for anorthite to 6 for the AL79 glass and the latter from 6 (for the AL20 glass) to 5.4 for albite. Regarding the network former intermixing, Fig. 14d shows that the amount of Si-O-Si bonds increases with the amount of silicon in the structure whereas the Si-O-Al and Al-O-Al bonds decrease with the substitution of Al with Si. All these data are shown in Tables 8 to 11 of the ESI.

The Young's and Bulk moduli of the six glasses simulated with BMP are reported in Table 12 of the ESI and Fig. 15 as a function of the concentration of sodium oxide.

The error associated with the Young's and Bulk moduli is within 2.4 GPa. Considering the error bars, we observe an almost linear decrease in both Bulk and Young Moduli increasing the fraction of sodium oxide in the system. This trend derives from the inter-atomic forces, which are also connected to cations field strength, and from the atomic density: the greater the cation field strength and atomic density, the higher are elastic moduli [51]. Fig. 15b shows that a linear correlation is found with the parameter E_{net} defined as follows:

$$E_{net} = \frac{1}{V_{cell}}\left[\sum_{i}^{cations} n_i \cdot CN_{iO} \cdot BE_{iO} \cdot m_i\right]$$

where V_{Cell} is the volume of the simulation box, n_i is the number of cations of the i-th species, CN_{iO} is the mean coordination number of the i-O pairs of atoms (i = Ca, Na, Si, and Al). BE_{iO} are the gas phase bond enthalpies for each type of bond in the corresponding molecules

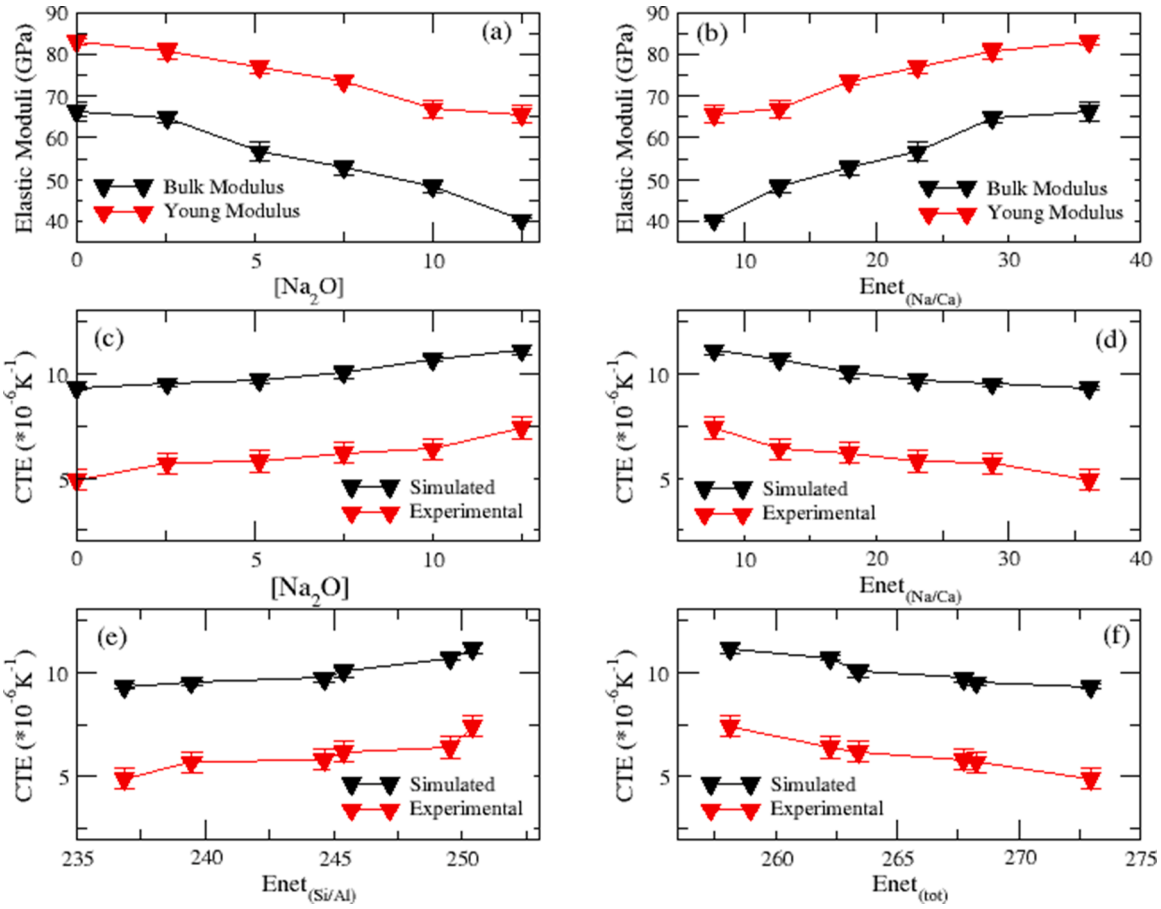

Fig. 15. (a) Elastic moduli as a function of sodium oxide concentration, (b) Elastic Moduli as a function of E_{net} computed using only Ca and Na ions, (c) CTE as a function of sodium oxide, (d) CTE as a function of E_{net} computed using only Ca and Na ions, (e) CTE as a function of E_{net} using only Si and Al, (f) CTE as a function of E_{net} computed using all the cations.

reported in ref [52]. and m_i are multiplicative factors that take into account the contribution to the overall degree of connectivity of the cations (1 for Na and 2 for Ca and average number of BO per Si and Al ions).

The fact that the elastic properties correlate well with this descriptor built only on the bases of Na and Ca ions means that their value is mainly governed by the relative strength of the Ca-O and Na-O bonds and the cohesive effect of the corresponding Ca and Na polyhedral. These properties depend on the substitution of Na with Ca. $E_{net}^{Ca/Na}$ decreases from 36.072 kJ/mol·Å^3 for anorthite to 7.729 kJ/mol·Å^3 for albite. The Na/Ca substitution leads to an increased cohesion of the glass and thus improved elastic properties. When E_{net} is computed using only Si and Al we observed an opposite trend, that is, $E_{net}^{Si/Al}$ increases of 10 kJ/mol·Å^3 going from anorthite to albite. Therefore, the substitution of Si with Al should reduce the elastic properties. However, this contribution is lower than that provided by Na/Ca substitution and the overall effect is an increase in the elastic moduli.

Panels c, d, and e of Fig. 15 shows the trend of both the simulated and experimental CTE with the Na_2O content and the E_{net} descriptors computed using only Na and Ca, only Si and Al, and all cations.

The experimental data shows that the CTE of the rigid plagioclase glasses on average increases with decreasing Albite content. That is, increasing Na_2O content.

An increasing trend is observed also for the simulated data when going from Anorthite to Albite glasses.

The CTE of rigid glasses is known to be due to the thermal vibration of the glass network. Therefore, in the rigid glasses state the CTE is mainly governed by the strength of the binding forces between cations and the surrounding oxygens.

The CTE of complex multicomponent glasses like the plagioclase glasses investigated here depends on the binding forces of all cations with oxygen ions. Small cations with high field strength exert stronger forces on the surrounding oxygens than large cations with lower field strength. As discussed for the elastic properties, the possible changes in the binding forces result from the partial replacement of Si^{4+} by Al^{3+} and the concomitant substitution of Na^+ by Ca^{2+}. Fig. 14 reveals that the CTE correlates with E_{net} but with an opposite slope with respect to elastic properties. It decreases with the density of the strength energy. As discussed for elastic properties, the dominant contribution is provided by the substitution of Na with Ca rather than Al with Si.

4. Conclusions

In this work, we have systematically evaluated different interatomic potential models available in the literature on the reproduction of structure, density, and thermomechanical properties of albite and anorthite crystals and glasses. The Core-Shell (CS) potential provides excellent results for the crystalline structure of Albite and Anorthite and equally satisfactory are the values returned by the structural analysis of the two glasses, with mention of the O-T-O angles in the short-range order. However, it shows many imperfections to describe mechanical properties, especially when dealing with glassy systems, where it is the potential that makes the greatest relative errors. Even for crystalline systems while correctly predicting the trends of the elastic moduli, it provides very different results in absolute values if compared to the experimental ones. The SHIK and Du potentials give good predictions for the two crystals: in particular, Du gives better results for the Albite

structure and mechanical properties (it is important to remember that SHIK reverses the experimental trend in the Young Modulus of Anorthite). The results of the structural analysis of the glass systems of the two potentials tend to be in good agreement with each other, but there are some fundamental differences: for anorthite, SHIK potential provides a significantly lower percentage of BOs compared to Du one; both in Albite and Anorthite SHIK predicts the highest percentage of aluminum Q^3, instead Du is in line with other potentials. As for the CTE, Du provides an opposite trend with respect to the experimental one. The PMMCS potential provides acceptable results for the structure and mechanical properties of the two crystals: anorthite structural parameters are better described than albite ones. The predictions for the glass structure of the two aluminosilicates are similar to those obtained by other potentials; however, there are fractions of BOs among the lowest, fractions of Al-O-Al bridges among the highest, and the lowest fraction of Si Q^4 in Anorthite compared to all the other force fields. The simulation of the mechanical properties of the two glasses provides acceptable values. BMP potential predicts with excellent accuracy the structural parameters of Albite (except for the Si-O-Si angles which are underestimated) and Anorthite; as long as it concerns mechanical properties it correctly reproduces the experimental trend but, similarly to other potentials, it provides absolute values that do not coincide with the reference ones. In the structural analysis of the two glasses, substantial differences from PMMCS can be noted: the percentage of BOs are among the highest, those of Al-O-Al bridges the lowest ever, and percentages of Q^4 species among the highest, more regular Si-O-Si angle distribution. The BMP potential has been used to investigate the effect of the cooling rate on the glass properties and the thermomechanical properties of glasses in the plagioclase series (albite-anorthite). We have shown that the CTE values extrapolated at the experimental cooling rates are in very nice agreement with experimental values. The error associated with the simulated CTE values reduces with the box dimensions and this property should be computed using simulation boxes containing at least 50k atoms. The decrease of the CTE values in the plagioclase series going from the Albite to Anorthite glass is due to the substitution of Na with Ca rather than the replacement of Si with Al.

CRediT authorship contribution statement

Annalisa Pallini: Methodology, Writing – original draft, Investigation. **Marco Bertani:** Writing – original draft, Methodology. **Daniel Rustichelli:** Investigation. **Benedikt Ziebarth:** Writing – review & editing, Funding acquisition. **Wolfgang Mannstadt:** Writing – review & editing, Funding acquisition. **Alfonso Pedone:** Conceptualization, Supervision, Writing – review & editing, Funding acquisition.

Declaration of Competing Interest

The authors declare that they have no known competing financial interests or personal relationships that could have appeared to influence the work reported in this paper.

Data availability

Data will be made available on request.

Acknowledgments

SCHOTT Inc. and the Department of Chemical and Geological Sciences of the University of Modena and Reggio Emilia are acknowledged for the partial financing of the Ph.D. scholarship of Annalisa Pallini.

Supplementary materials

Supplementary material associated with this article can be found, in the online version, at doi:10.1016/j.jnoncrysol.2023.122426.

References

[1] A.G. Schott, Thin, stable, anti-reflective, Interceram Int. Ceram. Rev. 68 (2019) 12–13.
[2] Y. Bottinga, D.F. Weill, The viscosity of magmatic silicate liquids; a model calculation, Am. J. Sci. 272 (1972) 438–475.
[3] A. Pedone, Properties calculations of silica-based glasses by atomistic simulations techniques: a review, J. Phys. Chem. C 113 (2009) 20773–20784.
[4] D. Presti, F. Muniz-Miranda, F. Tavanti, A. Pedone, Structure analysis and properties calculations. Atomistic Simulations of Glasses, John Wiley & Sons, Ltd, 2022, pp. 89–122, https://doi.org/10.1002/9781118939079.ch4.
[5] A. Pedone, M. Bertani, L. Brugnoli, A. Pallini, Interatomic potentials for oxide glasses: past, present, and future, J. Non-Cryst. Solids X 15 (2022), 100115.
[6] L. Deng, J Du, Development of boron oxide potentials for computer simulations of multicomponent oxide glasses, J. Am. Ceram. Soc. 102 (2019) 2482–2505.
[7] A. Pedone, G. Malavasi, M.C. Menziani, A.N. Cormack, U. Segre, A new self-consistent empirical interatomic potential model for oxides, silicates, and silica-based glasses, J. Phys. Chem. B 110 (2006) 11780–11795.
[8] M. Bertani, M.C. Menziani, A Pedone, Improved empirical force field for multicomponent oxide glasses and crystals, Phys. Rev. Mater. 5 (2021), 045602.
[9] S. Sundararaman, L. Huang, S. Ispas, W Kob, New interaction potentials for alkali and alkaline-earth aluminosilicate glasses, J. Chem. Phys. 150 (2019), 154505.
[10] A. Tilocca, N.H. de Leeuw, A.N Cormack, Shell-model molecular dynamics calculations of modified silicate glasses, Phys. Rev. B 73 (2006), 104209.
[11] P.H. Ribbe, H.D. Megaw, W.H. Taylor, R.B. Ferguson, R.J. Traill, The albite structures, Acta Crystallogr. B 25 (1969) 1503–1518.
[12] J.E. Wainwright, J Starkey, A refinement of the structure of anorthite, Z. Krist. Cryst. Mater. 133 (1971) 75–84.
[13] K. Masuda, Frictional properties of anorthite (feldspar): implications for the lower boundary of the seismogenic zone, Earth Planets Space 72 (2020) 135.
[14] M. Tribaudino, et al., Thermal expansion of plagioclase feldspars, Contrib. Mineral. Petrol. 160 (2010) 899–908.
[15] J. Arndt, F. Häberle, Thermal expansion and glass transition temperatures of synthetic glasses of plagioclase-like compositions, Contrib. Mineral. Petrol. 39 (1973) 175–183.
[16] Glasses: aluminosilicates - Archive ouverte HAL. https://hal.science/hal-03450045/.
[17] D. Wolf, P. Keblinski, S.R. Phillpot, J. Eggebrecht, Exact method for the simulation of Coulombic systems by spherically truncated, pairwise r−1 summation, J. Chem. Phys. 110 (1999) 8254–8282.
[18] W. Smith, T.R. Forester, DL_POLY_2.0: a general-purpose parallel molecular dynamics simulation package, J. Mol. Graph. 14 (1996) 136–141.
[19] M.P. Allen, D.J. Tildesley, Computer Simulation of Liquids, Oxford University Press, 2017.
[20] J.-.P. Ryckaert, G. Ciccotti, H.J.C Berendsen, Numerical integration of the cartesian equations of motion of a system with constraints: molecular dynamics of n-alkanes, J. Comput. Phys. 23 (1977) 327–341.
[21] S.V. Sukhomlinov, M.H. Müser, Determination of accurate, mean bond lengths from radial distribution functions, J. Chem. Phys. 146 (2017), 024506.
[22] A. Pedone, G. Malavasi, M.C. Menziani, U. Segre, A.N. Cormack, Molecular Dynamics Studies of Stress−Strain Behavior of Silica Glass Under a Tensile Load, ACS Publications, 2008, https://doi.org/10.1021/cm800413v. https://pubs.acs.org/doi/full/10.1021/cm800413v.
[23] G.N. Greaves, A. Fontaine, P. Lagarde, D. Raoux, S.J. Gurman, Local structure of silicate glasses, Nature 293 (1981) 611–616.
[24] T. Taniguchi, M. Okuno, T. Matsumoto, X-ray diffraction and EXAFS studies of silicate glasses containing Mg, Ca and Ba atoms, J. Non-Cryst. Solids 211 (1997) 56–63.
[25] C.D. Yin, M. Okuno, H. Morikawa, F. Marumo, T. Yamanaka, Structural analysis of CaSiO3 glass by X-ray diffraction and Raman spectroscopy, J. Non-Cryst. Solids 80 (1986) 167–174.
[26] A.C. Hannon, B. Vessal, J.M. Parker, The structure of alkali silicate glasses, J. Non-Cryst. Solids 150 (1992) 97–102.
[27] G.E. Brown, et al., EXAFS and NEXAFS studies of cation environments in oxide glasses, J. Phys. Colloq. 47 (1986) C8–661. -C8-668.
[28] P. Bhaskar, et al., Cooling rate effects on the structure of 45S5 bioglass: insights from experiments and simulations, J. Non-Cryst. Solids 534 (2020), 119952.
[29] H.-.I. Kim, S.K. Lee, Extent of disorder in iron-bearing albite and anorthite melts: insights from multi-nuclear (29Si, 27Al, and 17O) solid-state NMR study of iron-bearing NaAlSi3O8 and CaAl2Si2O8 glasses, Chem. Geol. 538 (2020), 119498.
[30] A. Atila, E.M. Ghardi, S. Ouaskit, A Hasnaoui, Atomistic insights into the impact of charge balancing cations on the structure and properties of aluminosilicate glasses, Phys. Rev. B 100 (2019), 144109.
[31] A. Pedone, E. Gambuzzi, M.C. Menziani, Unambiguous description of the oxygen environment in multicomponent aluminosilicate glasses from O-17 solid state NMR computational spectroscopy, J. Phys. Chem. C 116 (2012) 14599–14609.
[32] L. Cormier, D.R. Neuville, Ca and Na environments in Na2O–CaO–Al2O3–SiO2 glasses: influence of cation mixing and cation-network interactions, Chem. Geol. 213 (2004) 103–113.
[33] D.R. Neuville, L. Cormier, A.-.M. Flank, R.J. Prado, P. Lagarde, Na K-edge XANES spectra of minerals and glasses, Eur. J. Mineral. (2004) 809–816, https://doi.org/10.1127/0935-1221/2004/0016-0809.

[34] J. Marcial, J. McCloy, Role of short range order on crystallization of tectosilicate glasses: a diffraction study, J. Non-Cryst. Solids 505 (2019) 131–143.
[35] S.K. Lee, J.F. Stebbins, Al–O–Al and Si–O–Si sites in framework aluminosilicate glasses with Si/Al=1: quantification of framework disorder, J. Non-Cryst. Solids 270 (2000) 260–264.
[36] J.F. Stebbins, S.K. Lee, J.V.Letters Oglesby, Al-O-Al oxygen sites in crystalline aluminates and aluminosilicate glasses: high-resolution oxygen-17 NMR results, Am. Mineral. 84 (1999) 983–986.
[37] C.R.A. Catlow, A.R. George, C.M. Freeman, Ab initio and molecular-mechanics studies of aluminosilicate fragments, and the origin of Lowenstein's rule, Chem. Commun. (1996) 1311–1312, https://doi.org/10.1039/CC9960001311.
[38] A. Tilocca, Cooling rate and size effects on the medium-range structure of multicomponent oxide glasses simulated by molecular dynamics, J. Chem. Phys. 139 (2013), 114501.
[39] L. Deng, J Du, Effects of system size and cooling rate on the structure and properties of sodium borosilicate glasses from molecular dynamics simulations, J. Chem. Phys. 148 (2018), 024504.
[40] M. Okuno, F Marumo, The structures of anorthite and albite melts, Mineral. J. 11 (1982) 180–196.
[41] R. Knoche, D.B. Dingwell, S.L Webb, Non-linear temperature dependence of liquid volumes in the system albite-anorthite-diopside, Contrib. Mineral. Petrol. 111 (1992) 61–73.
[42] E.T. Chen, R.N. Barnett, U Landman, Crystal-melt and melt-vapor interfaces of nickel, Phys. Rev. B 40 (1989) 924–932.
[43] V.S. Dozhdikov, A.Yu. Basharin, P.R Levashov, Two-phase simulation of the crystalline silicon melting line at pressures from –1 to 3GPa, J. Chem. Phys. 137 (2012), 054502.
[44] Y. Zou, S. Xiang, C Dai, Investigation on the efficiency and accuracy of methods for calculating melting temperature by molecular dynamics simulation, Comput. Mater. Sci. 171 (2020), 109156.
[45] W. Sun, V. Dierolf, H. Jain, Molecular dynamics simulation of the effect of cooling rate on the structure and properties of lithium disilicate glass, J. Non-Cryst. Solids 569 (2021), 120991.
[46] X. Li, et al., Cooling rate effects in sodium silicate glasses: bridging the gap between molecular dynamics simulations and experiments, J. Chem. Phys. 147 (2017), 074501.
[47] M. Pota, et al., Molecular dynamics simulations of sodium silicate glasses: optimization and limits of the computational procedure, Comput. Mater. Sci. 47 (2010) 739–751.
[48] K. Vollmayr, W. Kob, K Binder, Cooling-rate effects in amorphous silica: a computer-simulation study, Phys. Rev. B 54 (1996) 15808–15827.
[49] A. Pedone, M.C. Menziani, A.N Cormack, Dynamics of fracture in silica and soda-silicate glasses: from bulk materials to nanowires, J. Phys. Chem. C 119 (2015) 25499–25507.
[50] A. Pedone, G. Malavasi, M.C. Menziani, U. Segre, A.N Cormack, Molecular dynamics studies of stress-strain Behavior of silica glass under a tensile load, Chem. Mater. 20 (2008) 4356–4366.
[51] A. Pedone, G. Malavasi, A.N. Cormack, U. Segre, M.C. Menziani, Insight into elastic properties of binary alkali silicate glasses; prediction and interpretation through atomistic simulation techniques, Chem. Mater. 19 (2007) 3144–3154.
[52] W.M. Haynes, CRC Handbook of Chemistry and Physics, 95th edition, CRC Press, 2014.